Scattering-Rate Approach for Vertical Electron Transport in III–V Quantum Cascade Heterostructures

zur Erlangung des akademischen Grades

doctor rerum naturalium

(Dr. rer. nat.)

im Fach Physik

eingereicht an der

Mathematisch-Naturwissenschaftlichen Fakultät

der Humboldt-Universität zu Berlin

von

M. Sc. Sergii Kurlov

Präsident der Humboldt-Universität zu Berlin

Prof. Dr.-Ing. Dr. Sabine Kunst

Dekan der Mathematisch-Naturwissenschaftlichen Fakultät

Prof. Dr. Elmar Kulke

Gutachter:

1. Prof. W. Ted Masselink
2. Prof. Henning Riechert
3. Prof. Jacob B. Khurgin

Tag der mündlichen Prüfung: 17.05.2018

Abstract

Since their invention in 1994, quantum cascade lasers (QCLs) have become the standard semiconductor laser source for the mid- and far-infrared spectral range. These unipolar devices are based on the population inversion between quantized subbands in biased semiconductor heterostructures. A useful theoretical model is essential for the optimization and further development of new QCL sources. A simple method for describing the electron transport in QCL is based on scattering rates between electron subbands. These can be described easiest using a phenomenological model with experimental or empirical parameters.

The main goal of this work is development of compact description of scattering processes in the frame of scattering-rate approach for the reliable prediction of temperature dependent characteristics of mid-infrared quantum cascade lasers. We start this work with a brief overview of semiconductor heterostructures and main intersubband scattering mechanisms for quantum cascade lasers. The resulting transition rates from initial states to another subbands are described by phonons and elastic scattering. Additionally, necessary modeling techniques are considered for simulation processes in QCLs using self-consistent scattering-rate model. Based on original work we introduce a simplified model for vertical electron transport between separated subbands at liquid nitrogen temperatures. In this approach the transition rate is written as the product of the overlap integral for the squared moduli of the envelope functions and a phenomenological factor that depends on the transition energy. The approach is reviewed and extended for a broad temperature range. There, the transition factor is derived and written for different scattering mechanisms separately. Then we analyze "so-called" T_0 characteristic for a number

of active region designs received from the calculations by present temperature dependent model and the experimental data.

Zusammenfassung

Seit ihrer Erfindung in 1994 haben sich Quantenkaskadenlaser (QCL) zu der Standard-Halbleiterlaserquelle im mittleren und weiten Infrarotspektrum entwickelt. Diese unipolaren Laser basieren auf der Populations-Inversion zwischen quantisierten sub-Bändern in Halbleiterheterostrukturen. Ein gutes theoretisches Modell ist essenziell für die Optimierung und weitere Entwicklung von neuen QCL Laserquellen. Eine einfache Methode, Elektronentransport in QCL zu beschreiben, stützt sich auf ein phänomenologisches Modell für die Streuraten zwischen elektronischen sub-Bändern. Das Hauptziel dieser Arbeit ist die Entwicklung eines kompakten Ansatzes für Streuraten für die effiziente Vorhersage der temperaturabhängigen Charakteristika von QCLs im mittleren Infrarotspektrum.

Die Arbeit beginnt mit einem kurzen Überblick über Halbleiterheterostrukturen und die wichtigsten Streumechanismen für Übergänge zwischen sub-Bändern in QCLs. Dabei sind elastische Übergänge sowie Phononenstreuung für die Übergangsraten zwischen verschiedenen sub-Bändern relevant. Ausserdem werden die notwendigen Modellierungstechniken für Simulationsprozesse in QCLs mit einem selbst-konsistenten Streuraten-Modell vorgestellt. In dieser Arbeit wurde ein vereinfachtes Modell für vertikalen Elektronentransport zwischen sub-Bändern bei der Temperatur von Flüssigstickstoff entwickelt. Die Übergangsrate ist in diesem Ansatz das Produkt des Überlappintegrals der quadrierten Moduli der einhüllenden Funktion und einem phänomenologischen Faktor, der von der Übergangsenergie abhängt. Der Übergangsfaktor wird für verschiedene Übergangsmechanismen einzeln hergeleitet, und eine Erweiterung des Modells auf einen breiten Temperaturbereich wird vorgestellt. Schliesslich analysieren wir die

sogenannte T_0-Charakteristik für einige Designs der aktiven Region, die aus Rechnungen mit vorhandenen temperaturabhängigen Modellen und experimentellen Daten gewonnen wurden.

Contents

1 Semiconductors and introduction to quantum cascade lasers

The goal of this chapter is to give introduction into physics of semiconductor heterostructures and quantum cascade lasers based on a light generation type by creation of electron inversion between subband energy levels in conduction band.

1.1 Semiconductor heterostructures

The semiconductors are materials with non zero energy bandgap and with temperature-dependent electrical resistivity in the range of $10^{-2} - 10^{9}\ \Omega \cdot cm$. Semiconductors occur in different chemical composition from elemental (Si, Se) to complicated ($Cd_{1-x}Mn_xTe$, La_2CuO_4). Silicon, germanium, and different II-IV, III-V compound semiconductors are the widely used in electronic devices. III-V compound semiconductors provide the material basis for a number of well-established commercial technologies, as well as new cutting-edge classes of electronic and optoelectronic devices. They are high-electron-mobility and heterostructure bipolar transistors, diode lasers, light-emitting diodes, photo-detectors, electro-optic modulators, frequency-mixing components *etc*. The operating characteristics of these devices depend critically on the physical properties of the constituent materials, which are often combined in heterostructures containing carriers confined to nanometer dimensions [17].

Figure 1.1(a) shows the relation between energy gap E_g and lattice constant a for III-V binary compound semiconductors which are attractive for optoelectronic devices and also for QCLs. A limited number of two compound semiconductors creates restrictions for

variation of the electrical characteristics of devices. Ternary compound semiconductors allow to extend the range of possible electronic band structures. The lines in Figure 1.1(a) show the relation between E_g and lattice constant a for ternary compounds $A_xB_{1-x}C$. The energy band structure for direct ternary compound InGaAs semiconductor is present in Fig. 1.1(b).

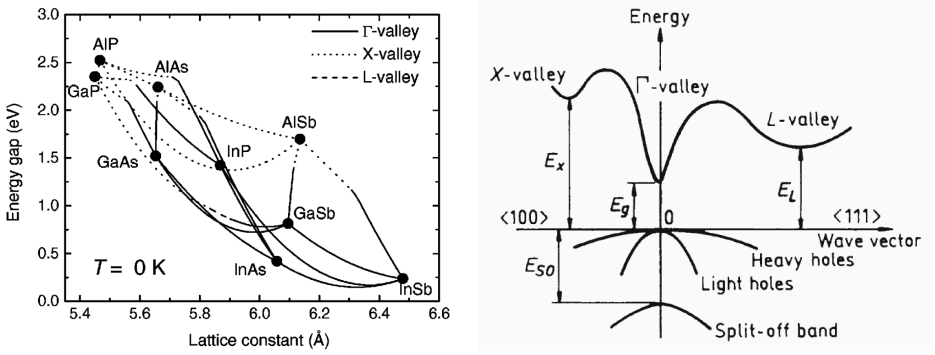

Figure 1.1: a) Lowest forbidden gap versus lattice constant at zero temperature for several of the more common semiconductors such as InGaAs, InAlAs, *etc* (Ref. [18]). The curves indicate Γ-, X-, and L-valley gaps by solid, dotted, and dashed lines, respectively.
b) Diagram of the band structure in the vicinity of the energy gap of InGaAs within the first Brillouin zone (Ref. [19]).

1.1.1 Semiconductor heterojunctions

Two layers of dissimilar crystalline semiconductors put in contact create heterojunction. Due to unequal band gaps the interface produces a step in energy band profile. Figure 1.2(a) shows 3 possible types of heterojunctions with the straddling, the staggered, and the broken gaps. The sandwich of different semiconductors creates the heterostructure with a number of heterojunctions. Heterostructures are characterized by the energy profiles of energy gap $E_g(z)$, conduction band $E_c(z)$, and valence band $E_v(z)$ which demonstrate the potential wells and the barriers in the growth direction z perpendicular to the interfaces (Fig. 1.2(b)).

In the case of equal lattice constants for contacting surfaces the heterostructure is called lattice-matched where the strain tensor $\bar{\varepsilon}$ is zero. If the lattice constants a_i are different,

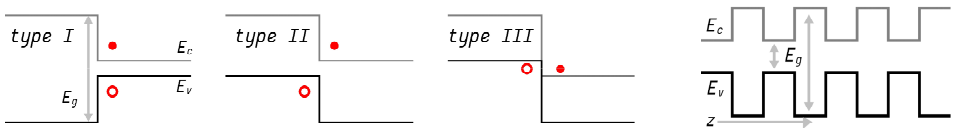

Figure 1.2: a) One-dimensional potentials for three types of semiconductor heterojunctions caused by band alignment. Electrons and holes are denoted by filled and open circles, respectively.
b) Configuration of *type I* creates a superlattice in the z direction.

the semiconductor layers and interfaces are strained. Strains change the energy band structure and the electronic properties of heterostructures. The discontinuities in valence and conduction bands at the semiconductor interfaces are essential for the analysis of the properties of any heterojunction. The calculation of band offsets at semiconductor interface can predict and explain properties of semiconductor heterostructures. Calculations based on local-density-functional theory and pseudo potentials have been carried out for a wide variety of lattice-matched and strained-layer interfaces [20, 21]. Unfortunately, the computational complexity of such calculations is very hard, that restricts their usage as a tool in the analysis and design of novel heterostructures. The self-consistent calculations are unfeasible for the case of a large strain, so several "model-solid" theories are applicable for a wide spectrum of heterojunctions and strains (see discussion in Ref. [21]).

1.1.2 Effective mass and envelope function approach

There are several models for the description of semiconductor band structure. These can be divided into two categories: theoretical and phenomenological models . The phenomenological models such as nearly free electron [22], pseudo-potential [23], $\mathbf{k}\cdot\mathbf{p}$ and Linear Combination of Atomic Orbitals [24] approaches, etc. use minimum parameters which must be obtained from experiment.

The effective mass approximation (multiband $\mathbf{k}\cdot\mathbf{p}$ method) is the most economical and useful description of the energy band structure in semiconductors. This section concentrates on this method because $\mathbf{k}\cdot\mathbf{p}$ method is opportune for interpreting optical spectra

and uses the energy gap E_g and optical matrix element Z. There is a minimal number of parameters for characterization of semiconductor that can be derived from optical measurements.

The **k**·**p** method can be obtained from the one-electron Schrödinger equation within Bloch theorem [17]:

$$\left(\frac{p^2}{2m}+\frac{\hbar\mathbf{k}\cdot\mathbf{p}}{m}+\frac{\hbar^2k^2}{2m}+V\right)\psi_{n,\mathbf{k}}=E_{n,\mathbf{k}}\psi_{n,\mathbf{k}}, \tag{1.1}$$

where wave vector **k** refers to first Brillouin zone, $\psi_{n,\mathbf{k}}$ and $E_{n,\mathbf{k}}$ are the wave function and eigenstate labeled by band index n. It follows from the Bloch theorem that the total wave function is $\Psi_{n,\mathbf{k}}=\exp(\imath\mathbf{k}\cdot\mathbf{r})\psi_{n,\mathbf{k}}(\mathbf{r})$ when an electron moves in a periodic potential.

For the wave vector**k** = 0 the one dimensional Schrödinger equation is reduced to:

$$\left(\frac{\hbar^2}{2m}\frac{\partial^2}{\partial z^2}+V(z)\right)\psi_{n,\mathbf{0}}(z)=E_{n,\mathbf{0}}\psi_{n,\mathbf{0}}(z), \tag{1.2}$$

where $\hbar\dfrac{\partial}{\partial z}$ denotes the electron momentum p.

From **k**·**p** method the effective mass of electron m* for small values of **k** can be written as [25]:

$$\frac{1}{m^*}=\frac{1}{m_0}+\frac{2}{m_0^2k^2}\sum_{n'\neq n}\frac{|\langle\psi_{n,\mathbf{0}}|\mathbf{k}\cdot\mathbf{p}|\psi'_{n,\mathbf{0}}\rangle|^2}{E_{n,\mathbf{0}}-E_{n',\mathbf{0}}} \tag{1.3}$$

where m_0 is the mass of free electron and $E_{n,\mathbf{k}}=E_{n,\mathbf{0}}+\frac{\hbar^2\mathbf{k}^2}{2m^*}$.

From this equation we can see that the electron mass is different in solid and for free electron. The electron in semiconductors has different mass due to coupling between electronic states in different bands via the **k**·**p** term.

The effective mass of electron has different values as a function of wave vector **k**:

$$m^*=\hbar^2\left(\frac{\partial^2E}{\partial k^2}\right)^{-1}. \tag{1.4}$$

In empirical 2-band model the effective mass of the electron m^* in the conduction band is given in terms of the band parameters:

$$\frac{m_0}{m^*} = (1+2F) + \frac{E_P(E_g + 2\Delta_{so}/3)}{E_g(E_g + \Delta_{so})}. \tag{1.5}$$

where F, E_P, Δ_{so} denote the Kane parameter, interband matrix element and spin-orbit splitting, respectively.

Energy gaps E_g in Γ-, X-, and L-valleys depend on temperature and their functional form can be fitted by the empirical Varshni formula [26]:

$$E_g(T) = E_g(0) - \frac{\alpha T^2}{T+\beta}, \tag{1.6}$$

where $E_g(0)$ denotes E_g at zero temperature. α and β are adjustable Varshni parameters (see Table 1.1).

For calculation of the conduction band edge we should know direct energy gap E_g, the average valence band $E_{\mathrm{v,\,av}}$, and the split-offsetΔ_{so} energies:

$$E_c = E_g + E_{\mathrm{v},av} + \frac{\Delta_{so}}{3}. \tag{1.7}$$

With all these parameters the diagram of the band structure near the center of Brillouin zone can be obtained (Fig. 1.3).

Other parameters for binary and compound semiconductors of III-V group can be found in [18]. For example, the band structure parameters for binary compound InAs, AlAs and GaAs are given in Table 1.1 and can be obtained in the effective mass approximation from experiments.

For the ternary alloys the dependence of the energy gap on alloy composition is assumed to fit a quadratic form:

$$E_g(A_{1-x}B_x) = (1-x)E_g(A) + xE_g(B) - x(1-x)C, \tag{1.8}$$

where the so-called bowing parameter C accounts for the deviation from a linear interpolation between the two binaries A and B.

Other parameters (Δ_{so}, a_c, etc.) have the same dependence as in Eq. 1.8 (non zero

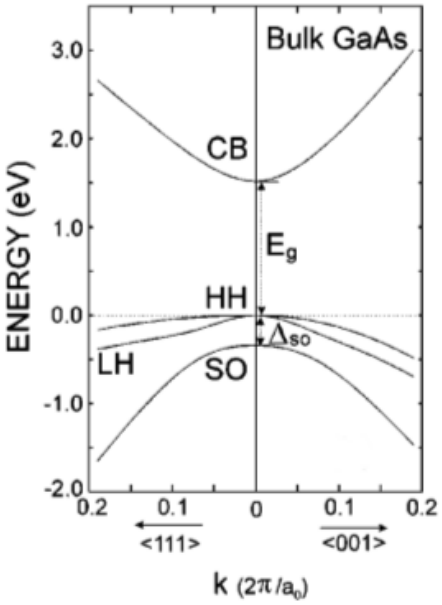

Figure 1.3: Diagram of the band structure near the center of Brillouin zone in GaAs bulk material (Ref. [22]).

Table 1.1: Band structure parameters for InAs, AlAs and GaAs binary alloys (Ref. [18])

Parameters	InAs	AlAs	GaAs
a_{lc} ($\AA$)	6.0583+ 2.74×10^{-5}(T-300)	5.661+ 2.90×10^{-5}(T-300)	5.65325+ 3.88×10^{-5}(T-300)
E_g^{Γ} (eV)	0.417	3.099	1.519
$\alpha(\Gamma)$ (meV/K)	0.276	0.885	0.5405
$\beta(\Gamma)$ (K)	93	530	204
Δ_{so} (eV)	0.39	0.28	0.341
$m_e^*(\Gamma)$	0.026	0.15	0.067
γ_1	20.0	3.76	6.98
γ_2	8.5	0.82	2.06
γ_3	9.2	1.42	2.93
E_p (eV)	21.5	21.1	28.8
F	-2.9	-0.48	-1.94
VBO (eV)	-0.59	-1.33	-0.80
a_c (eV)	-5.08	-5.64	-7.17
a_v (eV)	-1.00	-2.47	-1.16
c_{11} (GPa)	832.9	1250	1221
c_{12} (GPa)	452.6	534	566
c_{44} (GPa)	395.9	542	600

value) or by linear interpolation (zero value) and are presented in Table 1.2:

Table 1.2: Bowing parameters for GaInAs and AlInAs ternary alloys

Parameters	GaInAs	AlInAs
E_g^{Γ} (eV)	0.477	0.70
Δ_{so} (eV)	0.15	0.15
m_e^* (Γ)	0.0091	0.049
$\gamma_3 - \gamma_2$	0.481	0
E_P (eV)	-1.48	-4.81
F	1.77	-4.44
VBO (eV)	-0.38	-0.64
a_c (eV)	2.61	-1.4

Different semiconductor structures can be designed using this model in a good agreement with experiment.

1.1.3 Strain in heterostructures

As we wrote before strains influence to the band structure of semiconductor heterostructures.

Tensor of strain $\bar{\varepsilon}$ for semiconductor junction can be written in terms of parallel with and perpendicular to interface lattice constants, $a_{\parallel}$ and $a_{\perp}$, respectively:

$$\begin{aligned} \varepsilon_{i\parallel} &= \frac{a_{\parallel}}{a_i} - 1, & a_{\parallel} &= \frac{a_1 G_1 h_1 + a_2 G_2 h_2}{G_1 h_1 + G_2 h_2}, \\ \varepsilon_{i\perp} &= \frac{a_{i\perp}}{a_i} - 1, & a_{i\perp} &= a_i[1 - D_i(\tfrac{a_{\parallel}}{a_i} - 1)], \\ G_i &= 2(c_{11}^i + 2c_{12}^i)(1 - D_i/2), \end{aligned} \tag{1.9}$$

where h_i is thickness of $i^{th}-$ layer, G_i is the shear modulus. The variable D_i depends on the orientation of interface and elastic constant c_{11}, c_{12} and c_{44} as:

$$\begin{aligned} D^{001} &= 2\frac{c_{12}}{c_{11}}, \\ D^{110} &= \frac{c_{11} + 3c_{12} - 2c_{44}}{c_{11} + c_{12} + 2c_{44}}, \\ D^{111} &= \frac{c_{11} + 2c_{12} - 2c_{44}}{c_{11} + 2c_{12} + 4c_{44}}. \end{aligned} \tag{1.10}$$

For example in the case of (001) orientation of interface $D_i = D^{001}$ and $G_i = G^{001}$ etc.

With contact of substrate and first layer of heterostructure we have $h_1/h_2 \to \infty$, then $a_\parallel \to a_1$. The fractional volume change $\frac{\Delta\Omega}{\Omega}$ determines the hydrostatic contribution of the strain, and will enter the overall band lineups:

$$\frac{\Delta\Omega}{\Omega} = Tr(e) = (\varepsilon_{xx} + \varepsilon_{yy} + \varepsilon_{zz}) = 2\varepsilon_\parallel + \varepsilon_\perp. \tag{1.11}$$

The strain changes the values of valence E_v and conduction E_c bands and this deformations can be calculated as (Ref. [27]):

$$\Delta E_v = a_v \frac{\Delta\Omega}{\Omega}, \quad \Delta E_c = a_c \frac{\Delta\Omega}{\Omega}, \tag{1.12}$$

where a_v and a_c are the material constants for deformation of valence and conduction bands, respectively. With changing of valence band, the Δ_{so} value changes also for strained materials and corresponds to maximum of ($\Delta E_{v,i}$):

$$\begin{aligned} \Delta E_{v,1} &= -\frac{\Delta_0}{6} + \frac{\delta E_{001}}{4} + \frac{\sqrt{\Delta_0^2 + \Delta_0 \delta E_{001} + \frac{9}{4}(\delta E_{001})^2}}{2}, \\ \Delta E_{v,2} &= \frac{\Delta_0}{3} - \frac{\delta E_{001}}{2}, \\ \Delta E_{v,3} &= -\frac{\Delta_0}{6} + \frac{\delta E_{001}}{4} - \frac{\sqrt{\Delta_0^2 + \Delta_0 \delta E_{001} + \frac{9}{4}(\delta E_{001})^2}}{2}, \end{aligned} \tag{1.13}$$

where $\delta E_{001} = 2b(\varepsilon_\perp - \varepsilon_\parallel)$. The parameter b is the shear deformation potential for a strain which can be found in paper [27] or can be calculated by analyzing changes in the band structure when the strain is applied.

As a result the energy shift of valence band is:

$$\Delta E_v = a_v \frac{\Delta\Omega}{\Omega} + \frac{\Delta_0}{3} + \max(\Delta E_{v,1}, \Delta E_{v,2}, \Delta E_{v,3}). \tag{1.14}$$

Resulting band lineups at an AlSb/GaSb interface obtained from model-solid theory are shown in Fig. 1.4. For more information about the strains in semiconductor heterostructures see Ref. [27].

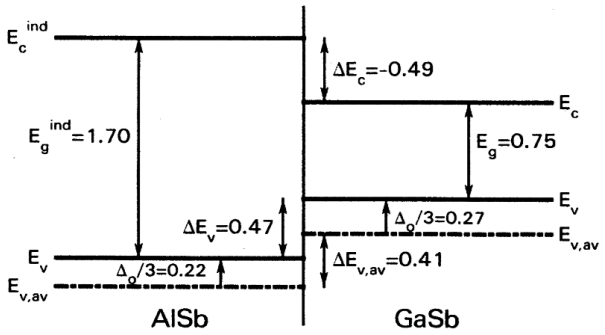

Figure 1.4: Band lineups at an AlSb/GaSb interface. The discontinuity in the average valence bands, $\Delta E_{v,av}$, is obtained from the model-solid theory. Spin-orbit splittings and energy gaps are taken from experiment. All energies are in eV [27]

.

1.2 Intersubband carrier transport and rate equation

The transition rate of electron from single initial $i_{\mathbf{k}}$ state to the states of final j level according to Golden Fermi's rule is given by [28]:

$$R_{i_{\mathbf{k}}j} = \frac{2\pi}{\hbar} \sum_{j_{\mathbf{k}'}} \left| \langle j_{\mathbf{k}'} | \widehat{H} | i_{\mathbf{k}} \rangle \right|^2 \delta(E_{j_{\mathbf{k}'}} - E_{i_{\mathbf{k}}} \mp \hbar\omega), \tag{1.15}$$

where $+/-$ corresponds to emission/absorption rate for inelastic processes with ω phonon frequency and for elastic scattering processes $\hbar\omega = 0$. $\widehat{H}$ denotes the time-dependent interaction potential which is different for dissimilar type of scatterings: elastic, inelastic, and carrier-carrier scatterings.

After averaging over carrier distribution the total transition rate between two levels is described by:

$$R_{ij} = \frac{\int R_{i_{\mathbf{k}}j} f_i^{\mathrm{FD}}(E) \left[1 - f_f^{\mathrm{FD}}(E \mp \hbar\omega)\right] \mathrm{d}E}{\int f_i^{\mathrm{FD}}(E)\, \mathrm{d}E}, \tag{1.16}$$

where $f_i^{\mathrm{FD}}(E)$ is the Fermi-Dirac distribution of electrons and for elastic scattering processes $\hbar\omega = 0$.

Investigated in this work n-type semiconductor devices are typically based on the direct band gap semiconductors. For them the electron transitions between the states are caused

mainly by inelastic (phonon scatterings), elastic (impurity, interface roughness, and alloy scatterings) and electron-electron scattering. The transverse optical phonon scattering is negligible at the Γ-point of the conduction band due to its spherical symmetry [29, 30]. Electron-electron scattering plays an important role only in the thermalization of the electron distribution within one period of the QCLs and does not participate in electron transport through cascades [31, 32].

1.2.1 Electron-phonon interaction

Phonons are quasiparticles of lattice vibration in a crystal. There are different modes of vibration in semiconductor: longitudinal and transverse acoustic, and longitudinal and transverse optical phonons. For QCLs the dominant phonon scattering is due to longitudinal optical (LO) phonons. Acoustic phonon play secondary role in scattering processes for QCLs.

Longitudinal optical phonon scattering

Harrison has derived (Ref. [33]) the following transition rate from initial $i_{\mathbf{k}}$ state to all states of final level j caused by electron-LO-phonon interaction:

$$R^{LO}_{i_{\mathbf{k}}j} = \frac{Y''}{2}\Theta\left(k_i^2 - \frac{2m^*\Delta}{\hbar^2}\right)\int_{-\infty}^{\infty}\frac{\pi|G_{ij}(K_z)|^2}{\sqrt{K_z^4 + K_z^2(2k_i^2 - \frac{2m^*\Delta}{\hbar^2}) + (\frac{2m^*\Delta}{\hbar^2})^2}}\,\mathrm{d}K_z, \tag{1.17}$$

where Y'' describes temperature dependence, $\Theta\left(k_i^2 - \frac{2m^*\Delta}{\hbar^2}\right)$ is Heaviside unit step function and $G_{ij}(K_z) = \int_{-\infty}^{\infty}\psi_j^*(z)\exp(-\imath K_z z)\psi_i(z)\,\mathrm{d}z$ is form factor. k_i denotes the in-plane electron wavevector and K_z the phonon wavevector perpendicular to the layer. $\Delta = E_j - E_i \pm \hbar\omega$, where the plus sign refers to the LO phonon emission and the minus sign to the LO phonon absorption.

The resulting scattering rate caused by electron - LO-phonon interaction, averaged over electron distribution in both the initial and final subbands of an infinitely deep GaAs quantum well is shown in Fig. 1.5.

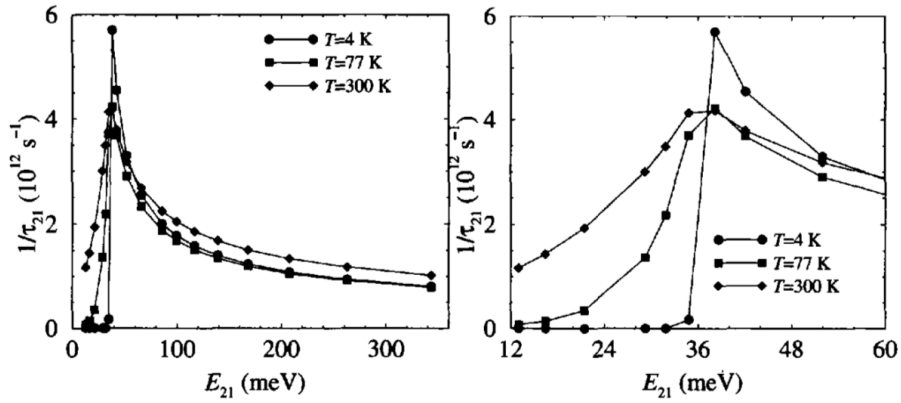

Figure 1.5: The mean scattering rate via the emission of LO phonons averaged over distributions in both the initial and final subband, as a function of the subband separation, shown for three different temperatures (Ref. [33]). Figure on the right shows zoomed area near LO-phonon energy.

.

The LO-phonon density increases as the temperature rises, thus increasing the scattering rate with phonon absorption.

Acoustic phonons

The acoustic electron interaction play secondary role in cascade structures like the QCLs, but due to the temperature dependence this scattering can't be neglected in electron transport in QCLs. The total transition rate from initial $i_{\mathbf{k}}$ state to the states of j level cost by acoustic phonon has form [34]:

$$R^{A}_{i_{\mathbf{k}}j} = \Xi^2 \frac{k_B T_L m^*}{\rho_c v_s^2 \hbar^3} \cdot \zeta, \tag{1.18}$$

where Ξ, ρ_c, and v_s are deformation potential, density, and longitudinal sound velocity, respectively. The overlap $\int dz \left|\psi_j(z)\right|^2 \cdot \left|\psi_i(z)\right|^2$ is denoted by ζ.

1.2.2 Elastic scatterings

It was shown last years that interface roughness scattering plays important role in the QCL operation [35, 36, 37]. Typically QCLs are low doped devices with a narrow region of donors in the injector wells. In this case impurity scattering plays the second role

for electron transitions in QCLs in comparison with other types of scattering, such as LO-phonon, acoustic phonon, and interface roughness scatterings.

Interface roughness scattering

Interface roughness scatterings (IFR) is the scattering on the no ideal interfaces between different semiconductors. Due to the temperature independent character of this type scattering the QCL performance can be changed significantly especially at low temperatures, when inelastic scatterings are "frozen" [38]. Interface roughness can be modeled as a random profile with Gaussian autocorrelation which is characterized by an average root-mean-square step height Δ and an in-plane correlation length Λ [39, 40].

The interface roughness scattering of the transition between two levels described by the envelope wave functions $\psi_i(z)$ and $\psi_j(z)$ at interfaces of quantum well can be written as [34, 41]:

$$R^{IFR}_{i_{\mathbf{k}}j} = \frac{m^*}{\hbar^3}\Delta^2\Lambda^2 \sum_l \delta U^2(z_l)\psi_j^2(z_l)\cdot\psi_i^2(z_l)\int_0^{\pi} d\phi\ \exp\left[\frac{-\Lambda^2 q^2(\phi)}{4}\right]\Theta\left[q^2(\phi)\right], \qquad (1.19)$$

where $\delta U(z_l)$ is the band offset at l^{th} interface, and $q^2(\phi) = 2k^2 + q_0^2 - 2k\sqrt{k^2+q_0^2}\cos\phi$ is the scattering vector in this process with $q_0^2 = 2m^*E_{ij}/\hbar^2$. The interface roughness height is characterized by mean square roughness $\Delta \approx 0.1$ nm and correlation length $\Lambda \approx 6.0$ nm for InGaAs/InAlAs/InP QCL structures. The value of Λ is a typical one for QCLs grown by molecular-beam epitaxy (MBE) and Δ_h can be calculated from the measured value $(\Lambda\Delta_h) = 0.6$ nm^2.

1.2.3 Resonant tunneling

Resonant tunneling is important scattering in the injector part of QCL, where electrons are transmitted from lower to upper laser level in next cascade. In first QCLs resonant tunneling was used as a main mechanism for pumping of upper laser level from ground level. Furthermore, Kazarinov and Suris describe idea of electron transport for light

amplification and generation by sequential resonant tunneling in superlattice [42].

The equation which describes resonant tunneling scattering rate is:

$$R_{ij}^{\text{tunnel}} = \frac{2|\Omega_{ij}|^2\tau_\perp}{1+\Delta^2\tau_\perp^2+4|\Omega_{ij}|^2\tau_\perp\tau_j}, \tag{1.20}$$

where $\tau_\perp$ is the in-plane dephasing time, $\hbar\Delta = E_i - E_j$ is the energy between levels, $2\hbar|\Omega_{ij}|$ is anti-crossing energy, and τ_i is a lifetime of i^{th} level.

1.2.4 Radiative intersubband transitions

The interaction between charge carriers and electromagnetic radiation is widely used in optoelectronic devices, especially in semiconductor lasers, photodiodes, and detectors. In this case electron transits between subband energy levels in one well with absorption or emission (stimulated and spontaneous) of photon. After the photon absorption the electron receives energy from photon and scatters to the upper level. For the photon emission there are two type of processes: spontaneous and stimulated. In spontaneous process emitted photon of energy between two subband ($\hbar\omega_{ij} = E_i - E_j$) can move in random direction without any phase relationship. In stimulated process an electron loses energy by the presence of electromagnetic radiation. The emitted photon is coherent with incident photon.

In 1917 Einstein introduced coefficients for description of spontaneous (A_{ij}) and stimulated emissions (B_{ij}), and absorption B_{ji}. The relations between Einstein coefficients are:

$$\begin{aligned} A_{ij} &= \frac{1}{\tau_{\text{sp}}} = \frac{e^2\omega^2 n_{\text{eff}}}{2\pi c^3\varepsilon_0 m^*}\left|f_{ij}\right|, \\ B_{ij} &= \frac{g_j}{g_i}B_{ji} = \frac{\pi^2 c^3}{\hbar\omega_{ij}^3}A_{ij}, \end{aligned} \tag{1.21}$$

where f_{ij}, n_{eff}, and g_i are the oscillator strength, the refractive index of medium, and the degeneracy of state i, respectively.

The photon radiative transition rate R_{ij}^{rad} between i^{th} and j^{th} subband levels ($E_i > E_j$)

can be written:

$$\begin{aligned} R_{ij}^{\text{rad}} &= A_{ij} + B_{ij} \cdot u, \\ R_{ji}^{\text{rad}} &= B_{ji} \cdot u. \end{aligned} \tag{1.22}$$

where u is the spectral energy density.

Generally the electron transport can be simply described by transition rates between the subband energy levels in conduction band. This type of gain medium description is widely applied to QCLs [43, 44, 45].

The total transition rate R_{ij} from i^{th} to j^{th} levels is a sum of individual non radiative photon scattering rates R^s and radiative transition rate R_{ij}^{opt}:

$$R_{ij} = R_{ij}^{\text{LO}} + R_{ij}^{\text{IFR}} + \ldots = \sum_s R_{ij}^s + R_{ij}^{opt}. \tag{1.23}$$

For a two level system the probability of scattering can be written as:

$$\begin{aligned} R_{21} &= \sum_s R_{21}^s + A_{21} + B_{21} \cdot u, \\ R_{12} &= \sum_s R_{12}^s + B_{12} \cdot u. \end{aligned} \tag{1.24}$$

Summarizing the rate equation for the i^{th} level can be written as

$$\frac{dn_i}{dt} = \sum_j n_j R_{ji} - n_i \sum_j R_{ij}, \tag{1.25}$$

where R_{ij} denotes the total scattering rate according to Eq. 1.23.

The solution of this equation system for all levels in structure gives the electron distribution for levels in the stationary states.

1.3 Overview of quantum cascade lasers

In this section we focused on the main QCL characteristics. Different designs of QCL active region will be discussed.

1.3.1 General principle

In 1971 Kazarinov and Suris proposed the idea of light amplification and generation in a semiconductor superlattice by electrons inversion in the lattice subbands [42]. The schematic structure for pumping of upper laser level and depopulation of lower laser level is present in Fig. 1.6. The light amplification may be achieved in coupled quantum well structure by population inversion in one quantum well. For coupled wave functions from adjacent (2_n and 3_{n+1}) quantum wells, the pumping is possible by resonant tunneling.

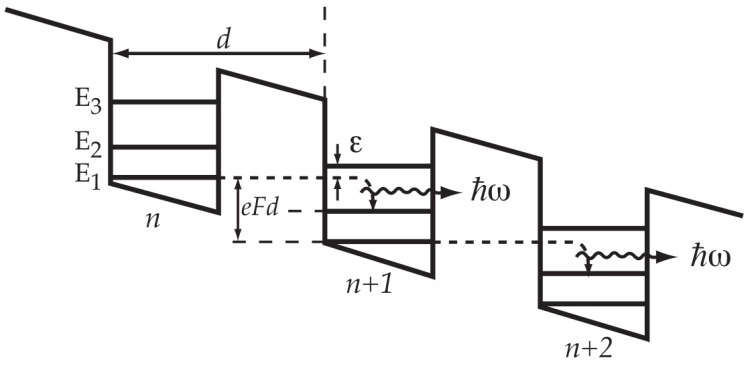

Figure 1.6: The schematic band structure of devices proposed by Kazarinov.

The main problem in realization of this proposal is operation in an unstable field region with negative differential resistance, that was demonstrated experimentaly [46]. The first experimental QCL was grown by MBE with the $Al_{0.48}In_{0.52}As$-$Ga_{0.47}In_{0.53}As$ heterojunction material system lattice matched to InP and demonstrated at low temperatures up to 88 K in 1994 by Faist *et al.* [1]. They appended the injector region between active regions for current stabilization and left unstable field region, which is shown in Fig. 1.7.

At present time schematically design of active region doesn't change significantly but different types of band structure were demonstrated. One of them is present in Fig. 1.8,

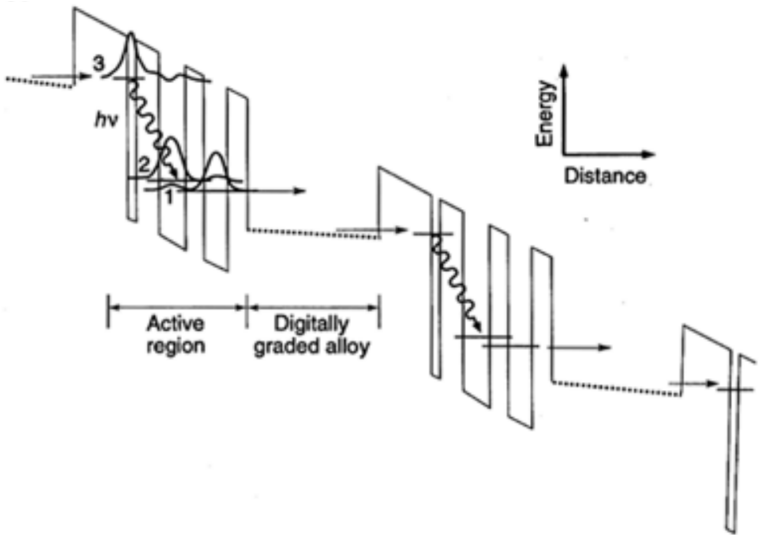

Figure 1.7: Conduction band energy diagram of a portion of a 25-cascade quantum cascade laser demonstrated by Faist *et al.* [1].

where the ground, upper, and lower laser levels are denoted by black, red, and blue color.

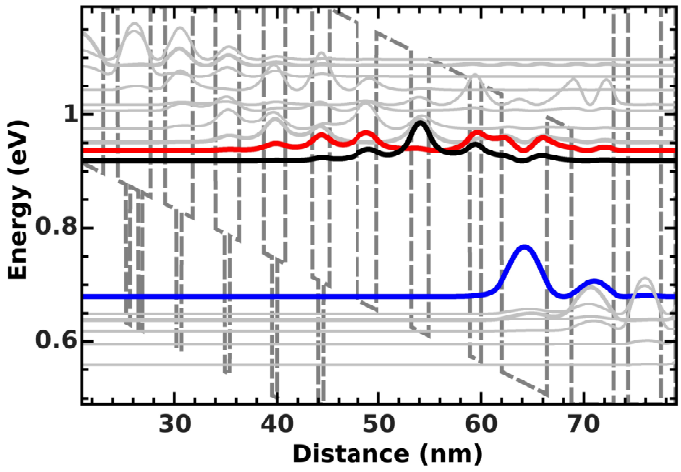

Figure 1.8: Conduction band profile (dashed line) for a mid-infrared QCL. The relevant energy states are displayed by gray solid lines. The ground, upper and lower laser levels are indicated by black, red, and blue bold solid lines, respectively.

1.3.2 Waveguide and optical gain

The active region of a quantum cascade laser is placed in the center of a mid-infrared waveguide forming a long ridge. Typical QCL geometry design is formed by the Fabry-

Perot cavity with $\sim 10-50\,\mu m$ width and 1-5 *mm* long ridge.

The QCL wafer processed into Fabry-Perot resonators acts, in the growth direction, as a dielectric waveguide with high refractive-index waveguide core and lower-refractive-index cladding layers which have low-absorption-index. The schematic QCLs resonator is present in Fig. 1.9. Cladding layer is grown over active region with low refractive index for the concentration of optical mode in active region. Active region is grown between InGaAs cladding layers for increasing of optical confinement factor in waveguide core. SiO_2 is deposited as insulator layer. Also InP:Fe can be used as lateral heat extraction layer due to the large heat and low electrical conductivities of this material.

Electrical field in resonator can be calculated from Maxwell's equations knowing optical parameters ($\alpha(\omega)$, $n(\omega)$) of materials for resonator and geometry of resonator created by these materials.

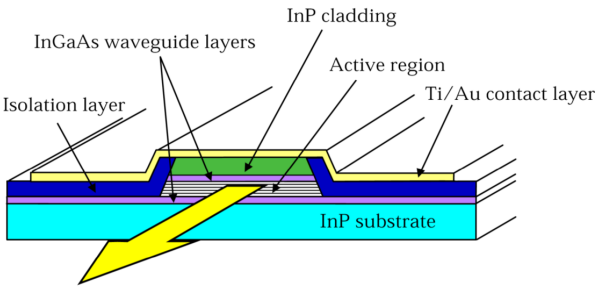

Figure 1.9: Schematic representation of a QCL ridge [47].

The solutions of stationary electric field created in a resonator are the optical modes. They can be represented as standing waves in waveguide. Few first transverse lasing modes for QCLs are illustrated in Fig. 1.10. Typically, in QCL resonator ridges the dominant mode is fundamental transverse mode.

The 1D distribution of electromagnetic field in transverse section of resonator is presented in Fig. 1.11.

This figure shows that optical mode is concentrated not only in active region. So optical confinement factor Γ is introduced as:

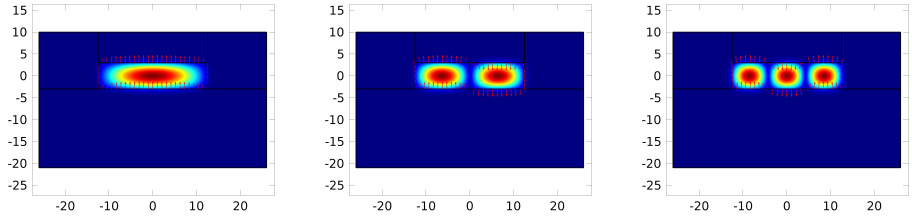

Figure 1.10: The surface plot visualizes the z-component of the electric field for TM_{00}, TM_{01}, TM_{02} modes.

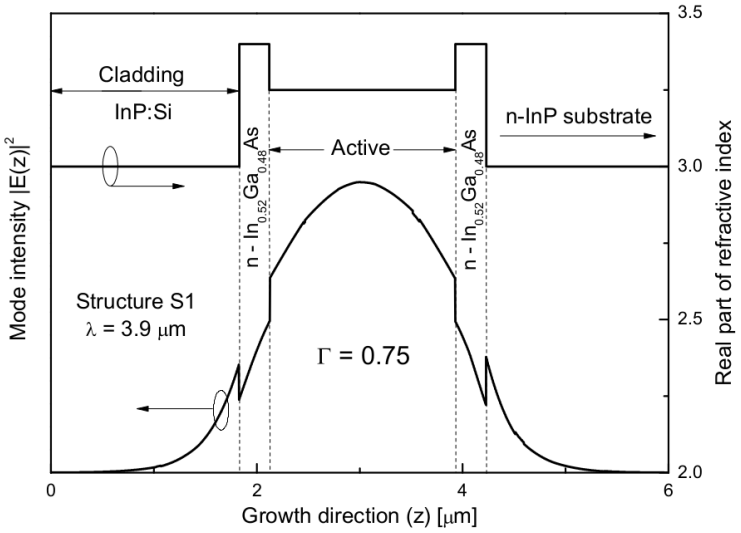

Figure 1.11: Optical mode along the direction of growth in gain medium.

$$\Gamma(\omega) = \frac{\int_{\text{act.reg.}} E^2(\omega, \mathbf{r})\, d\mathbf{r}}{\int E^2(\omega, \mathbf{r})\, d\mathbf{r}}, \tag{1.26}$$

where relation $\frac{\int_{\text{act.reg.}}}{\int}$ presents the concentration of electromagnetic field in an active region.

Typically optical confinement factor depends from the number of cascades and locates in range $\sim$30 % (10 cascade) - $\sim$70% (40). For the plasmon waveguide the optical confinement factor can be up to 99% in THz spectrum.

Differential gain g_d in the active region in simple form can be calculated from equation received by Faist for 3-level system [48]:

$$g_d = \tau_2 \left(1 - \frac{\tau_1}{\tau_{21}}\right) \frac{4\pi Z_{21}^2}{\lambda_0 \varepsilon_0 n_{eff} L_p} \frac{1}{2\gamma_{21}}, \tag{1.27}$$

where τ_2, τ_1, and τ_{21} are lifetimes of the upper 2 and lower 1 laser levels, and transition time between them, respectively. λ_0, Z_{21}^2, $2\gamma_{21}$, and L_p denote emitted wavelength, dipole matrix element of optical transition $< \psi_2|z|psi_1 >$, the measured value of the luminescence linewidth, and the length of one period, respectively.

1.3.3 Threshold current density

The main characteristics of laser devices such as threshold current, peak power, and slope efficiency can be experimentally received from power-current-voltage dependencies (Fig. 1.12).

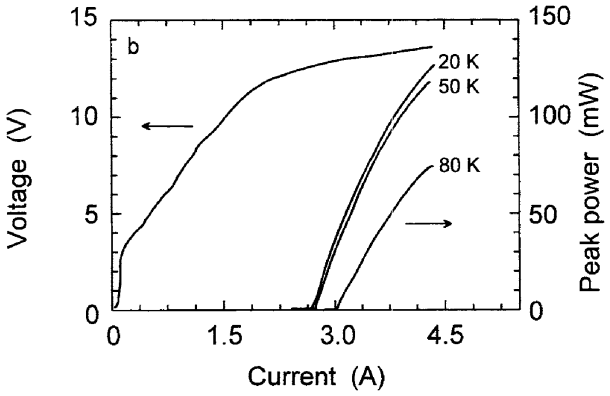

Figure 1.12: Pulsed light output and voltage versus current characteristics at various heat sink temperatures measured for a QCL with diagonal transition design of the active region.

Likewise these parameters can be calculated by various methods for calculation of carrier transport such as rate equations, Monte-Carlo, and 3D density matrix approaches. In the simplest case, the rate equations method is numerically very efficient. Often for the threshold current density and slope efficiency calculations the 3-level system is applicable:

$$\begin{aligned}
\frac{dn_1}{dt} &= -(R_{13}+R_{12})n_1 + R_{21}n_2 + R_{31}n_3 - I \\
\frac{dn_2}{dt} &= R_{12}n_1 - (R_{21}+R_{23})n_2 + R_{32}n_3 \\
\frac{dn_3}{dt} &= R_{13}n_1 + R_{23}n_2 - (R_{31}+R_{32})n_3 + I
\end{aligned} \tag{1.28}$$

where $R_{ij} = 1/\tau_{ij}$ is scattering rate from i to j levels and can include all scatterings which were described in previous section.

At threshold total losses α compensate gain $g\Gamma$ in the active region. The threshold current density J_{th} can be found from the relation between differential gain g_d, optical confinement factor Γ and total losses in medium α:

$$J_{th} = \frac{\alpha_m + \alpha_w}{g_d \Gamma}, \tag{1.29}$$

where all included variables were introduced and discussed above.

1.3.4 Classification of quantum cascade laser designs

Since the first demonstration of QCLs the different types of band structure (active region/injector) were demonstrated. Basically all the most representative QCL active regions can be sorted in few types.

Three quantum wells active regions The main difference from other designs is thin well between injector and active region. Active region consists of three quantum well in which the upper and lower laser levels are situated. The depopulation of lower laser level occurs by LO phonon scattering to the level down to lower laser level (Fig. 1.13). The energy between these levels is about of LO-phonon energy ($\sim$ 34 meV for AlInAs/GaInAs). The inversion of laser levels is achieved by this depopulation.

Depending on the width of injection barrier the 'vertical'[49] or 'diagonal' [50] transition can be achieved. Under vertical transition the photon scattering reduces to scattering within one direct quantum well.

For different thickness of thin quantum well between injector and active region the 'vertical' or 'diagonal' [50] transition is observed. For 'diagonal' transition the photon

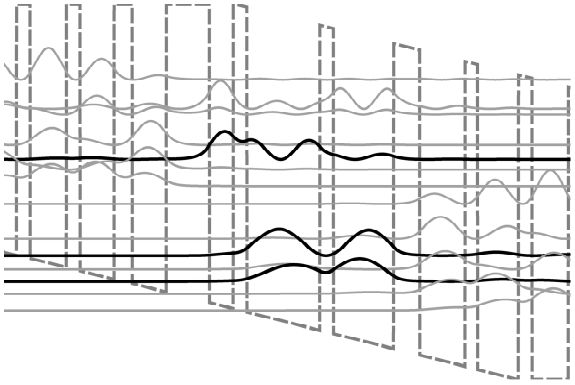

Figure 1.13: Schematic representation of the conduction band of a 3 quantum well active region. Laser levels are denoted by black solid lines.

scattering is achieved from 'lower' injector level to active region level.

Double phonon resonance active regions Next improved design is double phonon resonance active region. The decreasing of lower laser level is achieved by two phonon resonance [51]. In this active region (which is shown in Fig. 1.14) bellow the lower laser level the two next levels are located. The energy between these levels is in resonance with the energy of LO-phonon. In this case the electron depopulation is much efficiently.

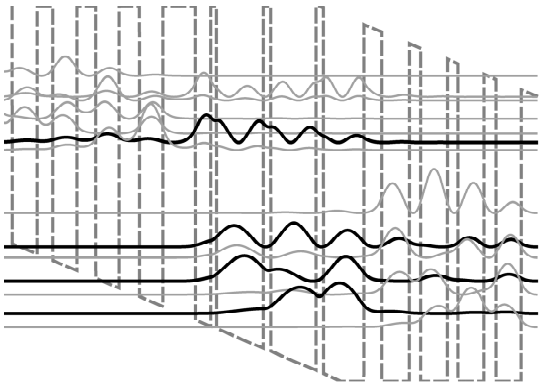

Figure 1.14: Schematic band diagram of a two-phonon resonance gain region designed for operation at $\lambda \sim 9\ \mu m$. The layer sequence of the structure, in nanometers, and starting from the injector barrier, is as follows: 4.0/1.9/0.7/5.8/0.9/5.7/0.9/5.0/2.2/3.4/1.4/3.3/1.3/3.2/1.5/3.1/1.9/3.0/2.3/ 2.9/2.5/2.9/ nm.

Bound-to-continuum active regions Bound-to-continuum designs [52] combine the advantages of the three-quantum well QCLs and of superlattice-QCLs (see bellow). In these devices, the lower laser state is localized at the upper edge of an injector/extractor miniband, which provides an efficient transport of electrons from the lower laser state to the injection barrier of the next active region (Fig. 1.15). The upper laser state is a single delocalized subband. At an appropriate positive bias, the fast intra-mini-subband scattering ($\tau \sim 0.1$ ps) leads to a rapid relaxation of electrons from upper to lower states within the miniband, thus favoring the efficient population inversion.

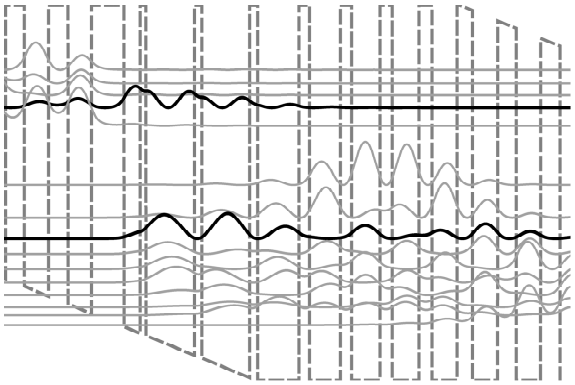

Figure 1.15: Schematic conduction band diagram of one stage of the structure under an applied electric field of $3.5 \cdot 10^4$ V/cm. The moduli squared of the relevant wave functions are shown.

Superlattice QCLs There is the latest type of QCLs which is observed in this section. In this QCLs the optical transition is observed between minibands in one active region (Fig. 1.16). In this case the overlap of minibands is large [53, 54]. Unfortunately, the increasing of overlap between minibands increases the leakage current that increases the threshold current in comparison with other types of QCL active regions.

In historical chronology the superlattice and three-quantum-well QCLs were created earlier. The subsequent improvement of these designs results in the bound-to-continuum QCL design.

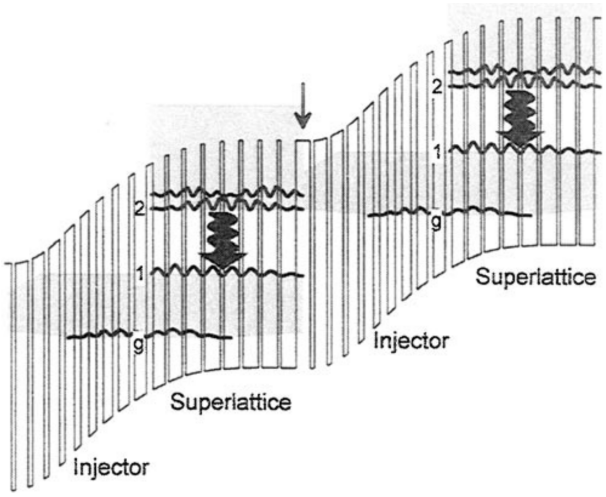

Figure 1.16: Schematic conduction-band structure of the original SL-QC laser. The laser transition between levels 2 and 1 (wavy arrow) is characterized by well delocalized electron wave functions, shown via their squared moduli([55]).

1.4 Summary

In this chapter we reviewed semiconductor characteristics, basic terminology for energy states and electron transport between them in semiconductor heterostructures. The introduction to QCL devices with presentation of their characteristics was done also. Finally, we discussed typical QCL active region configurations.

2 Simulation methods for quantum cascade lasers

In this chapter the necessary modeling technique for simulation processes in QCLs will be developed and tested. A useful theoretical model is essential for the optimization and further development of new QCL sources. Usually the simulation of QCLs devices starts with design of the electron states in the QCL heterostructures. The engineering of wave functions is important for definition of energy between upper and lower laser levels. Moreover bonding location of wave functions in active region influences on the pumping capacity of the upper laser level and depopulation of the lower laser level.

Next, the optical and nonradiative transitions between determined wave functions can be calculated by different carrier transport models, such as self-consistent rate equation approach. Self-consistent methods are useful with well known require material parameters, which are introduced in previous chapter. In this chapter we describes proposed phenomenological self-consistent scattering-rate model for the simulation of electron transport in mid-infrared quantum cascade lasers.

Further, this approach is applied to a number of MIR QCLs with a comparison of experimental data, such as power-current-voltage characteristics, temperature threshold current characteristic T_0, *etc*.

2.1 Solution of the one dimensional Schrödinger equation

Wave functions $\psi_i(E_i, z)$ and energy states E_i are determined by solving the one dimensional stationary Schrödinger equation. The analytic solution of Schrödinger equation 2.1 can be find for some of the most simple structures, such as finite few wells. For the QCL structures only numerical methods are applicable. One of simple but general practicable is the shooting method, which can be apply for energy dependent effective mass.

For this method the Schrödinger equation with boundary conditions is written as:

$$\begin{gathered}\left[-\frac{\hbar^2}{2m^*}\frac{\partial^2}{\partial z^2}+V(z)\right]\psi(z)=E\psi(z)\\ \psi(z),\frac{\partial\psi(z)}{\partial z}\to 0 \ \text{ at } \ z\to\pm\infty\end{gathered} \tag{2.1}$$

where $\hbar$ is the reduced Plank constant, m^* is the effective electron mass and $V(z)$ is the one dimensional potential.

For the numerical calculation the derivative $\frac{\partial\psi}{\partial z}$ may be rewritten as limit of the function ψ near z point:

$$\frac{\partial\psi}{\partial z}=\lim_{\delta z\to 0}\frac{\Delta\psi}{\Delta z}=\frac{\psi(z+\delta z)-\psi(z-\delta z)}{2\delta z} \tag{2.2}$$

where δz is the small partial step of z variable.

And the second derivative can be present as limit of derivative $\frac{\partial\psi}{\partial z}$:

$$\frac{\partial^2\psi}{\partial z^2}=\frac{\partial\psi/\partial z|_{(z+\delta z)}-\partial\psi/\partial z|_{(z-\delta z)}}{2\delta z} \tag{2.3}$$

After few simplification and substituting δz for $2\delta z$ the second derivation can be rewritten as:

$$\frac{\partial^2\psi}{\partial z^2}=\frac{\psi(z+\delta z)-2\psi(z)+\psi(z-\delta z)}{\delta z^2} \tag{2.4}$$

where $\psi(z-\delta z)$, $\psi(z)$ and $\psi(z+\delta z)$ are the values of ψ at the $z-\delta z$, z and $z+\delta z$ points, respectively.

With this approach equation 2.1 can be represented by:

$$-\frac{\hbar^2}{2m^*}\frac{\psi(z+\delta z)-2\Psi(z)+\psi(z-\delta z)}{\delta z^2}+(V(z)-E)\psi(z)=0 \tag{2.5}$$

Any $\psi(z+\delta z)$ value at $(z+\delta z)$ point can be found if previous $\psi(z)$, $\psi(z-\delta z)$ values are knowing at z and $(z-\delta z)$ points, respectively:

$$\psi(z+\delta z)=\left[\frac{2m^*}{\hbar^2}(\delta z)^2(V(z)-E)+2\right]\psi(z)-\psi(z-\delta z) \tag{2.6}$$

The transition energy for typical MIR QCLs based on InGaAs/InAlAs heterostructures can reach a few hundreds meV (up to 500 meV) when X and L valleys affect to electron condition in Γ valley. According to non parabolicity effect for MIR QCLs design the energy dependence of conduction band effective mass of electron can't be neglected and Schrödinger equation is written:

$$-\frac{\hbar^2}{2}\frac{\partial}{\partial z}\frac{1}{m^*(E,z)}\frac{\partial}{\partial z}\psi(z)+V(z)\psi(z)=E\psi(z) \tag{2.7}$$

For this case the value of $\psi(z+\delta z)$ can be written in form:

$$\begin{gathered}\frac{\psi(z+\delta z)}{m^*(E,z+\delta z/2)}= \\ \left[\frac{(2\delta z)^2}{\hbar^2}(V(z)-E)+\frac{1}{m^*(E,z+\delta z/2)}+\frac{1}{m^*(E,z-\delta z/2)}\right]\psi(z)-\frac{\psi(z-\delta z)}{m^*(E,z-\delta z/2)}.\end{gathered} \tag{2.8}$$

Taken into account the boundary conditions in the start of z axes $\psi(0)$ and $\psi(\delta z)$ should have zero and one or small values, respectively. With this conduction the value $\psi(z+\delta z)$ at any point can be found. The ψ value at the end of z environment should be zero according to the boundary conditions. By the shooting method the values of energy can be found for satisfy of boundary condition. The Newton-Raphson method improving the shooting method for finding ψ at the last point.

The effective mass in equation 2.8 can be present as $m^*(E)=m^*(0)[1+\alpha(E-V)]$ with

$\alpha = \left[1 - \frac{m^*(0)}{m_0}\right]^2 / E_g$, where $m^*(0)$ denotes the electron mass at the energy bandgap.

Received wave functions must be normalized as:

$$\psi(z) = \frac{\psi(z)}{\sqrt{\int_{-\infty}^{+\infty} \psi^*(z) \cdot \psi(z)\,\mathrm{d}z}} \quad \text{that} \quad \int_{-\infty}^{+\infty} \psi^*(z) \cdot \psi(z)\,\mathrm{d}z = 1 \tag{2.9}$$

Figure 2.1a shows numerically obtained wave functions with values of the ψ for the latest z point as a function of the energy (Figure 2.1b). The energy points with zero values is eigenvalue of Schrödinger equation. The wave functions without satisfaction of boundary condition is present on this figure for $E_1 - \delta E$ and $E_1 + \delta E$ energy, where δE is a small shift from eigenvalue E_1. For the improving of solution value the Newton's method is applicable.

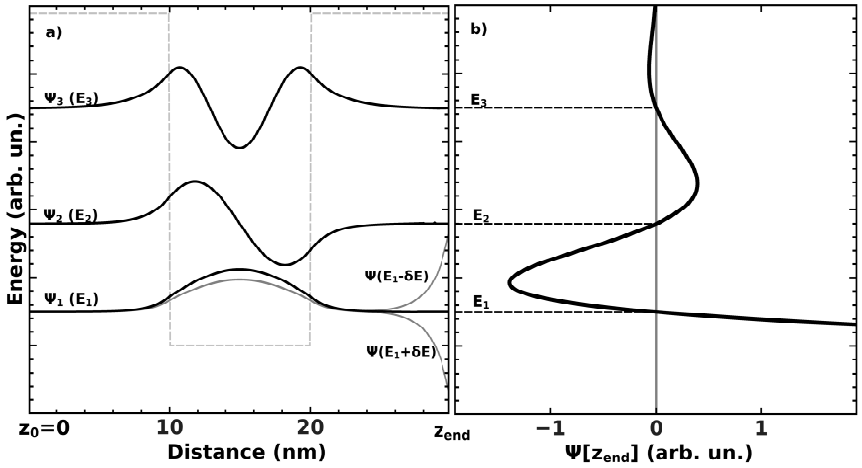

Figure 2.1: a) Schematic conduction band (dash line) of 10 nm *GaInAs* well between *AlInAs* barriers with few first wave functions ($\psi_1(E_1)$, $\psi_2(E_2)$, and $\psi_3(E_3)$) as solution of Schrödinger equation. $\psi(E_1 - \delta E)$ and $\psi(E_1 + \delta E)$ denote wave functions without satisfaction of boundary conditions and aren't eigenfunctions. b) Value of $\psi(z_{\text{end}})$ wave function of last z point (black solid line) as a function of energy. Vertical gray line denotes zero axes value of $\psi(z_{\text{end}})$ and concurrences of black and gray lines are solution of Schrödinger equation and present as horizontal dashed lines E_1, E_2, and E_3 for ψ_1, ψ_2, and ψ_3 wave functions, respectively.

2.2 Intersubband electron scattering rate model for quantum cascade lasers

2.2.1 Rate equation

For calculation of electron distribution and density current the rate equation with boundary condition for one period of QCL design with N wave functions can be solved.

To wright down correctly the periodical boundary conditions let us consider three periods of QCL active region with 3N wave functions (Fig. 2.2). We note, that the wave functions $j-N$, j and $j+N$ are equivalent except the shift Δz in real space, where Δz is the thickness of one cascade.

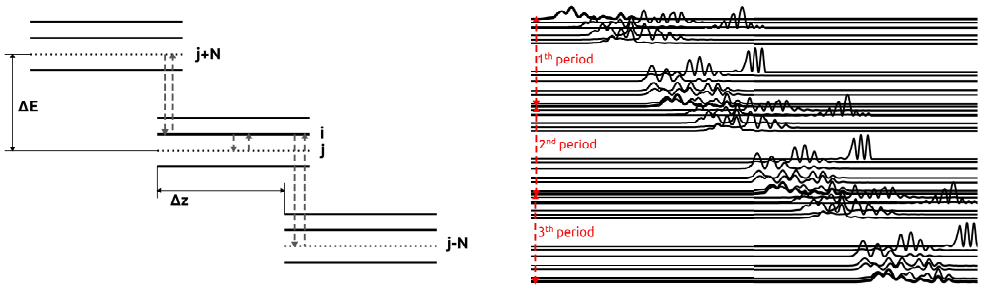

Figure 2.2: (a) Three schematic periods of a QCL - structure for electron distribution calculation.
(b) More realistic representation of squared moduli of relevant wave functions for three periods of QCL active region.

Rate equations can be written for one close period with N wave functions without current between other periods as:

$$\frac{dn_i}{dt} = \sum_{j=1}^{N} R_{ji} n_j - n_i \sum_{j=1}^{N} R_{ij} \tag{2.10}$$

where n_i is the population of $i-N$, i and $i+N$ equivalent levels.

Boundary conditions should be included in rate equation for current calculation and real electrons transport in QCL with large period numbers as:

$$\frac{dn_i}{dt} = \sum_{j=1}^{N} R_{ji} n_j - n_i \sum_{j=1}^{N} R_{ij} + \delta I_{i+} - \delta I_{i-} \tag{2.11}$$

where δI_{i+} are electrons coming into i level of this period and δI_{i-} are electrons coming out of i level of this period into levels of another periods.

We assume that electrons can not undergo transition over one and more periods. I.e. we consider electrons scattering only within a period and between the adjacent periods.

$$\delta I_{i+} = \sum_{j=1}^{N} n_{j+N} R_{j+N,i} + \sum_{j=1}^{N} n_{j-N} R_{j-N,i} \tag{2.12}$$

And for electron scattering from i level to another periods we write:

$$\delta I_{i-} = n_i \textstyle\sum_{j=1}^{N} R_{i,j+N} + n_i \sum_{j=1}^{N} R_{i,j-N} \tag{2.13}$$

where the first part of sum is transition from i level to next period and second part of sum is transition to previous period.

Full rate equation with boundary conditions for i level in period is:

$$\begin{gathered} \tfrac{dn_i}{dt} = \textstyle\sum_{j=1}^{N} R_{ji} n_j - n_i \sum_{j=1}^{N} R_{ij} + \\ + \textstyle\sum_{j=1}^{N} n_{j+N} R_{j+N,i} + \sum_{j=1}^{N} n_{j-N} R_{j-N,i} - \\ n_i \textstyle\sum_{j=1}^{N} R_{i,j+N} - n_i \sum_{j=1}^{N} R_{i,j-N}. \end{gathered} \tag{2.14}$$

Finally, the system of rate equations for $3N$ wave functions in three periods with N states in each period can be written as:

$$\begin{gathered} \tfrac{dn_i}{dt} = \textstyle\sum_{j=1}^{N} n_j [R_{ji} + R_{j+N,i} + R_{j-N,i}] - \\ - n_i \textstyle\sum_{j=1}^{N} [R_{ij} + R_{i,j+N} + R_{i,j-N}], \end{gathered} \tag{2.15}$$

where n_i is the electron sheet density n_i^{2D} in level i. Levels j, $j-N$ and $j+N$ are equivalent wave functions in first, second and third cascades, respectively, (see Fig. 2.2). In Eq. (2.15) the first term of the sum collects scattering contributions populating level i from the other $3N-1$ levels and the second term represents the contributions depopulating this

level to the other $3N-1$ levels.

The current density can be determined by:

$$J = \sum_{i,j=1}^{N} n_i[\phi_{ij}R_{ij} - R_{i,j+N} + R_{i,j-N}], \tag{2.16}$$

with $\phi_{ij} = 1,-1,0$ for transition of electrons from left to right, from right to left, or far away from any virtual interface.

2.2.2 The optical gain and photon-induced transition rate

Previously we wrote the rate equation system where the radiative transitions R_{ij}^{ph} can be included as:

$$R_{ij} = R_{ij}^{*} + R_{ij}^{ph} \,, \tag{2.17}$$

where R^{*} denotes nonradiative scattering rates. In the simplest case R^{*} can be written in empirical approach, in other cases as a sum of rates for various scattering mechanisms.

Generally optical transition rate can be written by terms of Einstein coefficients. For QCLs the nonradiative transition is faster then optical transition by spontaneous emission, so only the stimulated optical transition is included as an scattering event in gain medium. The rate R_{ij}^{ph} is proportional to optical intensity for corresponding mode at ω frequency. As usually only fundamental transverse mode for ω frequency is dominant and we will take into account only one mode in calculation:

$$R_{ij}^{ph} = |Z_{ij}|^2 \frac{\pi e^2}{c n_{eff} \varepsilon_0} \sum_{\omega} \Gamma I(\omega) L_{ij}(\omega), \tag{2.18}$$

where Γ is the optical confinement factor for fundamental mode, $I(\omega)$ and $L_{ij}(\omega)$ denote the light intensity and the Lorentzian line shape at the corresponding ω frequency. The Lorentzian line shape function for electron transition between i and j levels at ω frequency is given by:

$$L_{ij}(\omega) = \frac{1}{2\pi} \frac{\gamma_b}{\left(\hbar\omega - E_{ij}\right)^2 + \left(\gamma_b/2\right)^2}, \tag{2.19}$$

here $\gamma_b = \gamma_i + \gamma_j + \gamma_0$ determined by life time broadening i^{th} and j^{th} levels with broadening parameter γ_0 [56]. This parameter γ_0 is used for homogeneous broadening in a simplified way for elastic scatterings, such as interface roughness scattering.

In addition to rate equation written as Eq. 2.15 the intensity rate equations written as:

$$\frac{n_{eff}}{c} \frac{\partial I(\omega)}{\partial t} = \Gamma g(\omega) I(\omega) - \alpha I(\omega), \tag{2.20}$$

have to be iterated by a coupled approach. The steady state solution will be with $\frac{\partial I(\omega)}{\partial t} = 0$ condition which corresponds to $I(\omega) = 0$ or non zero value of intensity for the laser emitting, when $\Gamma g(\omega)$ gain will be equal to α losses in the gain medium.

The gain contribution at frequency ω is given by:

$$g(\omega) = \frac{\pi e^2 \omega}{c\varepsilon_0 n_{eff} L_p} \sum_{ij}^{E_i > E_j} (n_i - n_j)|Z_{ij}|^2 L_{ij}(\omega), \tag{2.21}$$

where L_p denotes period length.

For various goals the optical gain with photon transition rate can be used in different way. In the simplest case only optical gain is calculated at the steady state with $R_{ij}^{ph} = 0$ and without additional iterations. Then we will receive gain-current density-voltage characteristic. It good way for improving optical characteristics for recently received QCL design by changing different material parameters. From other hand, we could use gain-current density characteristic for determination of threshold current density J_{th}, when gain is equal to losses in laser stripe ($g\Gamma = \alpha$). This method we will apply for our model in the next sections.

2.2.3 Compact phenomenological scattering-rate model for low temperatures

As we wrote previously that the scattering rate model can use experimental or empirical input parameters as transition rate between energy level. A bottom-up approach is to begin with experimental results and describe them using a phenomenological model. Such a scattering-rate model has been developed for terahertz (THz) QCLs [44]. In this approach, several non-radiative scattering mechanisms including scattering via optical and acoustic phonons, electron-electron interaction, and scattering at ionized impurities are written in terms of the squared modulus of the dipole matrix element $|Z_{ij}|^2$, which is calculated for intersubband radiative transitions, and a function $F(E_{ij})$ that only depends on the transition energy E_{ij}. The total scattering rate between subbands i and j is given by $F(E_{ij})|Z_{ij}|^2$. Such a description has the advantage of including several scattering mechanisms in a compact form, allowing a straightforward modeling of charge carrier transport. Furthermore, the strategy uses measured data, ensuring accuracy at least within some range of application. The approach was demonstrated using a number of THz QCL designs that were modeled; very good agreement with experimental results in terms of current-voltage characteristics and gain spectra were reported [44, 56].

In case of THz QCLs, the role of scattering of electrons with longitudinal optical (LO) phonons is reduced due to the much larger LO phonon energy (E_{LO}) relative to the radiative transition energy. Therefore, the energy dependent factor $F(E_{ij})$ is taken to be constant for the range of energies of the order and above E_{LO}, which is a reasonable assumption for THz QCLs. However, the energy dependence of $F(E_{ij})$ for $E_{ij} > E_{\mathrm{LO}}$ becomes important for MIR QCLs with transition energies significantly larger than E_{LO}, reflecting the increased role of LO phonon interaction [36, 57].

Furthermore, while LO phonon scattering becomes the dominant scattering mechanism in MIR QCLs, the total non-radiative scattering rate is no longer driven by the dipole matrix element. Motivated by this, we replace the dipole matrix element used in the previous work by the overlap integral of the moduli squared of the envelope functions,

which is a more appropriate indicator for LO phonon scattering.

The proportionality factor between the overlap integral and the total non-radiative scattering rate will be denoted by $\rho(E_{ij})$. The energy dependence of this factor for energies more than E_{LO} is obtained from a phenomenological fit of published lifetimes of MIR QCLs. As a result, the function $\rho(E_{ij})$ appears to be quite "universal" for given material, allowing any MIR QCL to be simulated. Once the exchange terms for all transitions have been calculated, the simulation becomes significantly less onerous than including all scattering mechanisms.

Scattering-rate model

The electron transitions between the states in QCLs are caused mainly by inelastic (acoustic and LO phonons), elastic (alloy, interface roughness, and impurity), and electron-electron scattering [34]. Electron-electron scattering plays an important role only in the thermalization of the electron distribution within one period of the MIR QCLs [31, 32] and the transverse optical phonon scattering is negligible at the Γ-point of the conduction band due to its spherical symmetry [29, 30]. Alloy [58] and acoustic phonon scattering [59] can be approximated by a linear dependence on the wave function overlap ζ:

$$\zeta_{ij} = \int dz \, |\psi_i(z)|^2 |\psi_j(z)|^2 \,, \tag{2.22}$$

for the i^{th} and j^{th} bound states. However, these scattering effects typically play a secondary role in QCLs.

At low temperatures, the electron transport is driven by phonon emission and temperature-independent processes as IFR scattering. The role of IFR in low temperature luminescence has been analyzed in Refs. [13, 36, 38, 60]. In this phenomenological model IFR will be included into broadening parameter γ_0.

As next we focus on the electron transport through LO-phonon emission, as this mechanism plays a protagonic role in low-temperature intersubband scattering for large

($E_{ij} > E_{LO}$) intersubband energy spacing. The main contribution to the current density in QCL structures originates from scattering between electrons and LO phonons. According to Eq. 1.16 and Ref. [33], the average scattering rate R_{ij}^{LO} can be written in wave vector k -terms by

$$R_{ij}^{LO} = \frac{1}{\tau_{ij}} = \frac{\int_0^\infty dk\ k\ f_i(k) R_{ij}^{LO}(k)}{\int_0^\infty dk\ k\ f_i(k)}\ , \tag{2.23}$$

where f_i denotes electron distribution of the i^{th} subband. $R_{ij}^{LO}(k)$ is the LO-phonon transition rate of electrons from a state with momentum k in the initial i^{th} subband to a state in the j^{th} subband. This scattering rate is given by

$$\begin{aligned} R_{ij}^{LO}(k) &= \pi Y'' \Theta\left(k^2 + \tfrac{2m^*\Delta_{ij}}{\hbar^2}\right) \int_0^\infty dK_z \frac{\left|G_{ij}(K_z)\right|^2}{\sqrt{K_z^4 + 2K_z^2\left(2k^2 + \tfrac{2m^*\Delta_{ij}}{\hbar^2}\right) + \left(\tfrac{2m^*\Delta_{ij}}{\hbar^2}\right)^2}} \\ &= \pi Y'' \Theta\left(k^2 + \tfrac{2m^*\Delta_{ij}}{\hbar^2}\right) \int_0^\infty dK_z\ F(K_z, k)\ . \end{aligned} \tag{2.24}$$

Here k denotes the in-plane electron wavevector and K_z the phonon wavevector perpendicular to the layer. Θ denotes the step function, and Y'' describes the temperature dependence which will be observed in detail in temperature model. $\Delta_{ij} = E_i - E_j \mp E_{\mathrm{LO}}$, where the minus sign refers to LO phonon emission and the plus sign to LO phonon absorption. At low temperatures, we neglect the LO phonon absorption, because the thermal population of the phonon modes is negligible.

The modulus squared of the form factor:

$$|G_{ij}(K_z)|^2 = \int dz dz' \psi_i(z) \psi_i^*(z') \exp\left[-iK_z(z-z')\right] \psi_j^*(z) \psi_j(z')$$

restricts the probability of scattering in k space.

In general, the LO phonon scattering according to Eq. (2.24) cannot be completely described by a linear dependence on the wave function overlap ζ_{ij}. Nevertheless, such a linear dependence appears to be an appropriate approximation for many QCL structures. For a typical MIR QCL design [61, 62], Fig. 2.3(a) shows the calculated dependence of

the modulus squared of the form factor $|G_{ij}(K_z)|^2$ for the main laser transitions.

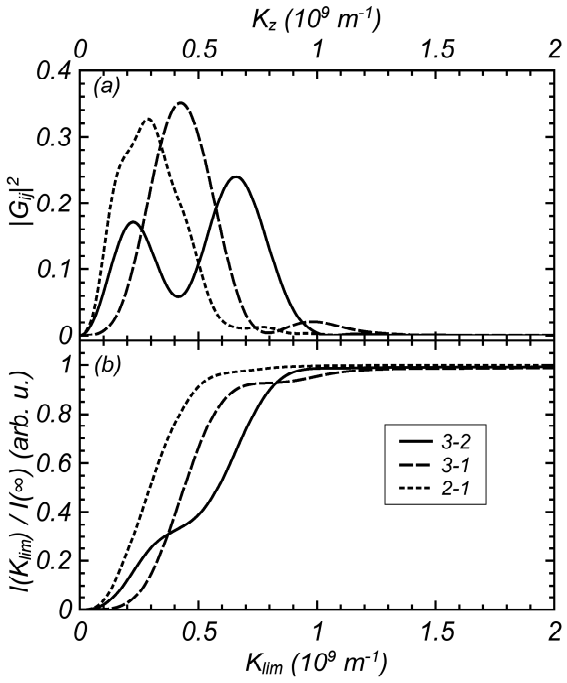

Figure 2.3: (a) Form factor $|G_{ij}(K_z)|^2$ and (b) the ratio of integrals $I(K_{\rm lim})$ to $I(K_{\rm lim}=\infty)$ according to Eq. (2.25) for the indicated transitions for a typical MIR QCL design [61]

.

For $K_z \gg 10^9$ m^{-1} and more large values, the form factor can be approximate to zero. In Fig. 2.3(b), the expression

$$I(K_{\rm lim}) = \int_0^{K_{\rm lim}} dK_z F(K_z, 0) \tag{2.25}$$

is shown as a function of the upper limit $K_{\rm lim}$. For $K_z > 10^9$ m^{-1}, $I(K_{\rm lim})$ saturates, implying that the main part of integral $\int_0^\infty dK_z F(K_z,0)$ in Eq. (2.24) results from the integration over region $(0, K_{\rm lim})$. However, if $\Delta_{ij} \gg 0$, the expression:

$$\frac{1}{\sqrt{K_z^4 + 2K_z^2\left(2k^2 + \frac{2m^*\Delta_{ij}}{\hbar^2}\right) + \left(\frac{2m^*\Delta_{ij}}{\hbar^2}\right)^2}}$$

is practically constant for these K_z values. In this case, it can be taken out of the integral in Eq. (2.24). We then obtain

$$R_{ij}^{LO}(k) = \pi Y'' \frac{\Theta\left(k^2 + \frac{2m^*\Delta_{ij}}{\hbar^2}\right) \int_0^{K_{\lim}} dK_z |G_{ij}(K_z)|^2}{\sqrt{K_{\lim}^4 + 2K_{\lim}^2\left(2k^2 + \frac{2m^*\Delta_{ij}}{\hbar^2}\right) + \left(\frac{2m^*\Delta_{ij}}{\hbar^2}\right)^2}} . \tag{2.26}$$

While the integrand $|G_{ij}(K_z)|^2$ tends to zero beyond $K_{\lim}$, the upper limit of the integral can be extended to ∞. In this case

$$\int_0^{K_{\lim}} dK_z |G_{ij}(K_z)|^2 \approx \int_0^{+\infty} dK_z |G_{ij}(K_z)|^2 = \pi\zeta_{ij}. \tag{2.27}$$

For energies higher than E_{LO}, the value of $k^2 + \frac{2m^*\Delta_{ij}}{\hbar^2}$ is always positive, and Eq. (2.26) becomes

$$R_{ij}^{LO}(k) = \pi Y'' \frac{\pi\zeta_{ij}}{\sqrt{K_{\lim}^4 + 2K_{\lim}^2\left(2k^2 + \frac{2m^*\Delta_{ij}}{\hbar^2}\right) + \left(\frac{2m^*\Delta_{ij}}{\hbar^2}\right)^2}} . \tag{2.28}$$

For the case of low temperatures and high energies between energy levels, when $m^*\Delta_{ij}/\hbar^2 \gg k^2$, Eq. (2.28) reduces to

$$R_{ij}^{LO}(0) = \frac{\pi^2 Y''/K_{\lim}^2}{1 + \frac{2m^*}{\hbar^2 K_{\lim}^2}\Delta_{ij}}\zeta_{ij}. \tag{2.29}$$

Although the above derivation strictly holds only for $\Delta_{ij} \gg 0$, we approximate the LO phonon scattering by a linear dependence on the wave function overlap for the entire range of E_{ij} values. Because in the MIR region the scattering rate $R_{ij}^{LO}(k)$ is practically independent of k, Eq. (2.23) becomes

$$R_{ij}^{LO} = \frac{\rho^{\mathrm{LO}}(E_{\mathrm{LO}})}{1 + a(E_{ij} - E_{\mathrm{LO}})}\zeta_{ij} = \rho^{\mathrm{LO}}(E_{ij})\zeta_{ij} , \tag{2.30}$$

where $\rho^{\mathrm{LO}}(E_{\mathrm{LO}}) = \pi^2 Y''/K_{\lim}^2$, $a = 2m^*/(\hbar^2 K_{\lim}^2)$, and

$$\rho^{\mathrm{LO}}(E_{ij}) = \frac{\rho^{\mathrm{LO}}(E_{\mathrm{LO}})}{1 + a(E_{ij} - E_{\mathrm{LO}})} . \tag{2.31}$$

In order to justify this approximation also for energy values $E_{ij} < E_{\mathrm{LO}}$, the energy dependence of $\rho^{\mathrm{LO}}(E_{ij}) = R_{ij}/\zeta_{ij}$ obtained from the calculated scattering rates R_{ij} accord-

ing to Eq. (2.23) are shown for two typical MIR and one THz QCL designs in Fig. 2.4.

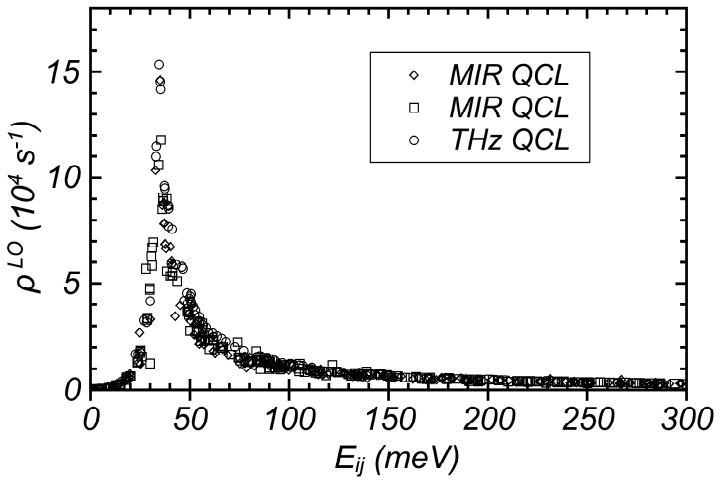

Figure 2.4: The values of $\rho^{\mathrm{LO}}(E_{ij})$ as a function of E_{ij} for a two typical MIR [61, 62] and one THz [63] QCL designs.

The dependence of ρ^{LO} on E_{ij} can be separated in two parts, one for energies below and one for energies above the LO phonon energy. The energy dependence of ρ^{LO} for $E < E_{\mathrm{LO}}$ can be described by a Fermi-Dirac distribution for $E_{ij} - E_{\mathrm{LO}}$, whereas for $E > E_{\mathrm{LO}}$ it can be approximated by $\rho^{\mathrm{LO}}(E_{ij})$ defined in Eq. (2.31).

In the spirit of Ref. [44], we now subsume all processes into one single equation using Eqs. (2.30) and (2.31) with the fit parameter a in units of meV^{-1}. We may expand this approach to energies below E_{LO} by replacing ρ^{LO} by ρ given in Ref. [44].

The energy-dependent factor $\rho(E_{ij})$, which subsumes non-radiative scattering processes in QCLs, is described by the empirical expression:

$$\begin{aligned}\rho(E_{ij}) &= \frac{\rho_0(E_{ij})}{2}\left[\exp(A_1)\left[1-\Phi(A_2)\right]+1+\Phi(A_3)\right] \\ &\times \left[1+k_{\mathrm{LO}}\left(1+\Phi(A_4)+E_0\frac{\Gamma}{(E_{ij}-E_{\mathrm{LO}})^2+\Gamma^2}\right)\right], \qquad (2.32)\end{aligned}$$

where

$$A_1 = \frac{E_{ij}}{E_a} + \frac{\sigma^2}{2E_a}\,, A_2 = \frac{E_{ij}}{\sqrt{2}\sigma} + \frac{\sigma^2}{\sqrt{2}E_a^2}\,, A_3 = \frac{E_{ij}}{\sqrt{2}\sigma}\,, A_4 = \frac{E_{ij} - E_{\mathrm{LO}}}{\sigma_s}\,. \tag{2.33}$$

and

$$\rho_0(E_{ij}) = \frac{2000\,|E_{ij}|}{E_{\mathrm{LO}}}\left(1 + \frac{\bar{a}E_{\mathrm{LO}}}{\bar{b}E_{ij}^2 + \bar{c}E_{\mathrm{LO}}} - \frac{\bar{a}}{\bar{b}E_{\mathrm{LO}} + \bar{c}}\right),\ \left[c^{-1}\right] \tag{2.34}$$

The parameters $E_a = 10.0$ meV, $\sigma = 5.0$ meV, $\Gamma = 5.0$ meV, and $E_0 = 10.0$ meV describe thermal activation, interface roughness, broadening, and strength of the LO phonon resonance, respectively. Furthermore, $\sigma_s = 2.0$ meV and $k_{\mathrm{LO}} = 25.0$ denote the width and magnitude of the the step-like increase of $\rho(E_{ij})$ at the LO phonon resonance, respectively. $\Phi(x)$ denotes the error function. The parameters $\bar{a} = 10$, $\bar{b} = 2$ meV^{-1}, and $\bar{c} = 0.1$ with a correction factor of 2000 c^{-1} lead to scattering rates similar to the ones in (In,Ga)As/(In,Al)As QCLs. The scaling factor $\rho_0(E_{ij})$ in the approximation of Ref. [44] is constant and equal to $\rho_0(E_{\mathrm{LO}})$ for the region of energies higher than E_{LO}. In our consideration, this factor $\rho_0(E_{ij})$ is energy dependent and takes the form of Eq. (2.35).

In contrast to Ref. [44], where the focus was on transitions with energies below or near the LO phonon energy, the wave function depending contribution is now the overlap ζ_{ij} rather than the dipole matrix element. Finally, the transition rate R_{ij}^{cpm} from i^{th} level to j^{th} level received for compact phenomenological model can be written:

$$R_{ij}^{cpm} = \begin{cases} \rho(E_{ij})\zeta_{ij} & \text{for } E_{ij} \le E_{LO} \\ \dfrac{\rho(E_{ij})\zeta_{ij}}{1 + a(E_{ij} - E_{\mathrm{LO}})} & \text{for } E_{ij} > E_{LO} \end{cases} \tag{2.35}$$

Using literature data for values of R_{ij} corresponding to different intersubband transitions in QCLs and calculating the corresponding overlap integrals ζ_{ij}, the prefactors of ζ_{ij} in Eq. (2.35) are reconstructed. The respective results are shown in Fig. 2.5 for the fit parameter $a = 0.0494$ meV^{-1}.

Using the Schrödinger equation, the full set of wave functions for the system under consideration is determined by shooting method. Based on this, the charge distribution

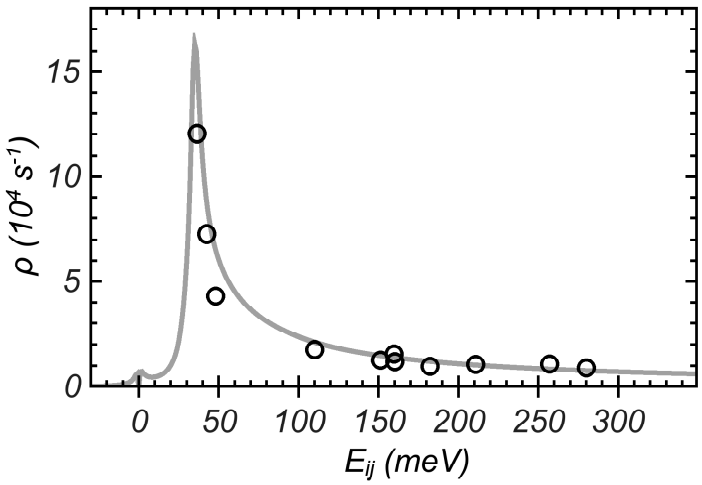

Figure 2.5: Prefactors of ζ_{ij} in Eq. (2.35) as a function of the transition energy E_{ij} for QCLs based on (In,Ga)As/(In,Al)As heterostructures. The open symbols represent the values of R_{ij}/ζ_{ij} for various $In_{0.52}Al_{0.48}As/In_{0.53}Ga_{0.47}As$ samples reported in the literature.[49, 61, 62, 64, 65, 66, 67] The solid line is a fit to the data.

and current density can be obtained solving the full system of rate equations for $3N$ wave functions in three periods with N states in each period. This system has the form such as Eq. 2.15:

$$\frac{dn_i}{dt} = \sum_{j=1}^{N} n_j[R^*_{ji} + R^*_{j+N,i} + R^*_{j-N,i}] - n_i \sum_{j=1}^{N} [R^*_{ij} + R^*_{i,j+N} + R^*_{i,j-N}] \,, \tag{2.36}$$

where $R^*_{ij} = R^{cpm}_{ij} + R^{ph}_{ij}$ denotes the full scattering rate from the i^{th} to the j^{th} level, which includes non-radiative transitions R^{cpm}_{ij} (Eq. 2.35) and radiative transitions R^{ph}_{ij} Eq. 2.18.

Simulation results for MIR QCLs

We apply our model to a broadband QCL at low temperature (80 K). The QCL design is based on the $In_{0.52}Al_{0.48}As/In_{0.53}Ga_{0.47}As$ heterostructure with *AlAs* barriers in the active region to minimize the carrier leakage.

The band structure of this QCL is shown for two different field strengths in Figs. 2.6(a) and 2.6(c). As a result of the self-consistent calculations using Eq. (2.36), we obtain the electron sheet densities n_i for the different electron subbands i as shown in Figs. 2.6(b)

and 2.6(d).

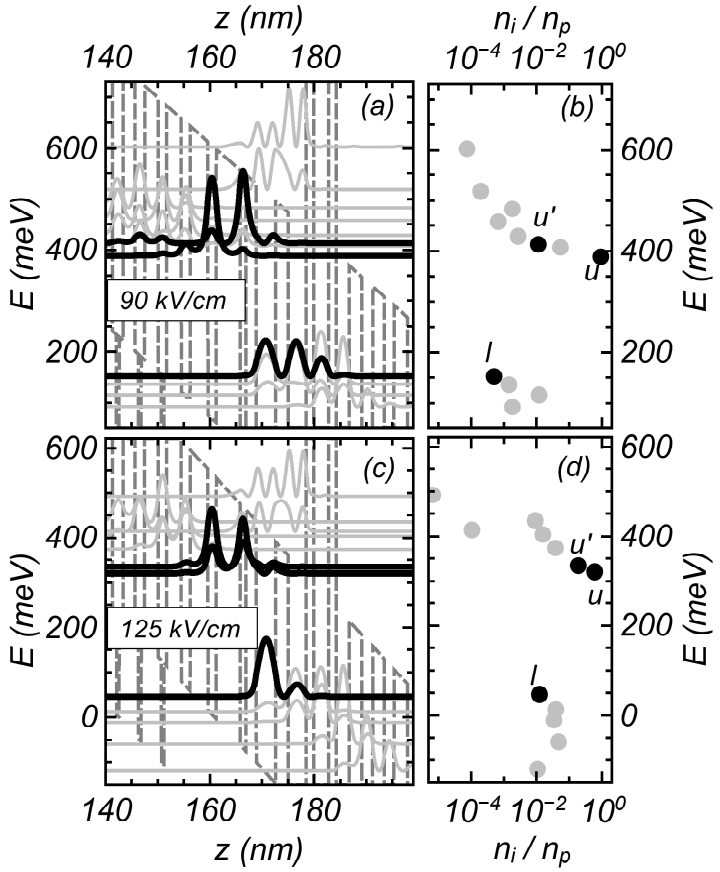

Figure 2.6: (a) The conduction band profile of the investigated QCL for an applied electric field of 90 kV/cm at threshold and (c) for 125 kV/cm at the maximum of the emitted power. The layer thicknesses in nm from left to right starting from the widest active region quantum well are 3.4/*1.6*/4.6/*1.1*/2.0/*3.7*/2.4/*3.5*/**1.4**/*0.7*/***0.4***/*0.7*/***0.4***/*0.7*/**1.4**/*1.0*/***0.5*** /*1.0*/2.4/*0.8*/***0.5***/*0.8*/2.2/*0.7*/***0.5***/*0.7*/2.6/*0.6*/***0.5***/*0.5*/2.8/*1.7*, where the $In_{0.52}Al_{0.48}As$ layers are denoted by regular, the $In_{0.53}Ga_{0.47}As$ layers by italic, the AlAs layers by bold, and the InAs layers by bold italic font. Underlined layers are *n*-doped resulting in a sheet density per period of $n_p = 2.5\ .\ \times 10^{11}$ cm^{-2}. Only relevant Wannier-Stark levels are shown. u, u', and l are the moduli squared of the wave functions of the two upper laser levels and the lower laser level, respectively. (b) and (d) show the corresponding average two-dimensional sheet density n_i/n_p for the different levels resulting from self-consistent calculation of the rate equations for 90 kV/cm and 125 kV/cm, respectively. A heat sink temperature of 80 K is assumed.

For a comparison of the results of the simulations with experimental data, we have

grown a 40-staged structure by gas-source molecular beam epitaxy, which has been processed into 25 μm-wide ridges using conventional optical lithography and wet chemical etching. A 0.5 μm-thick SiO_2 layer was deposited by reactive magnetron sputtering for electrical insulation of the sidewalls. Cr/Au contacts were evaporated for the top metallization.

Laser chips with uncoated facets of several resonator lengths L were mounted epilayer upon Cu holders for definition of the experimental wave guide losses α_w which can be extracted from linear dependence of the threshold current J_{th} to a inverse value of the cavity length $1/L$. This expression may be written as:

$$J_{th}\left(\frac{1}{L}\right) = \frac{\alpha_w + \alpha_m(L)}{g_d\Gamma} = \frac{\alpha_w}{g_d\Gamma} - \frac{ln(R)}{g_d\Gamma}\cdot\frac{1}{L}, \tag{2.37}$$

where mirror losses $\alpha_m = -\frac{ln(R)}{L}$ with the facet reflectivity $R = 0.3$.

Furthermore, laser chips with different length is used for obtaining real dependence of current density - voltage for QCL structure.

Figure 2.7 shows (asterisks) the typical optical power-current density $P-J$ and electric field-current density $J-V$ curves measured for a 25 μm-wide and 4.0 mm long devise which was mounted in a liquid nitrogen cryostat and driven by 500 ns pulses with a duty cycle of 0.5% at heat sink temperature of 80 K. Besides the electric field-current density characteristics calculated according to Eq. (2.16) and the optical power-current density characteristics calculated according to Ref. [34, 56] are shown by the dots in Figure 2.7.

For the calculations, we used the following parameters: mirror losses $\alpha_m = 3$ cm^{-1} and optical confinement factor $\Gamma = 0.7$. These parameters were determined by the finite element calculations for a 0.025×4.0 mm^2 device. The waveguide loss $\alpha_w = 2.5$ cm^{-1} was extracted from experiments follow Eq. 2.37. Additional fitting parameters in this model are the sheet-density per cascade $n_p = 2.5 \times 10^{11}$cm^2 and $\gamma_0 = 2.5$ meV, where γ_0 is a broadening parameter to accurately describe the spectral line shape $L_{ij}(\omega)$ (Eq. 2.19). Generaly, the correction factor γ_0 can be found from electro luminescence data [38, 68] or, as in this work, used as a fitting parameter in order to integrate scattering processes

that are not included in Eq. 2.32 into calculations.

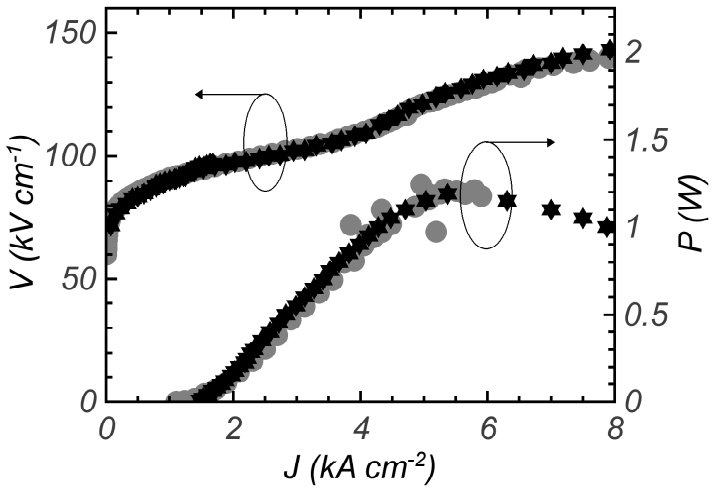

Figure 2.7: Measured (asterisks) and calculated (dots) electric field-current density and optical power-current density characteristics for a 0.025×4.0 mm^2 device. The device was driven by 500 ns current pulses with a duty cycle of 0.5% at a heat sink temperature of 80 K.

The observed weak "kink" around 4 kA cm^{-2} is related to the particular wave function alignment around 115 kV/cm (just before roll-over), which results in a resonance between levels u and u'. Due to a numerical effect, the calculated optical power–current density characteristic becomes high noisy after the laser roll- over (maximum of emitted power) and is omitted in Fig. 2.7. It is important to point out that using a rate equation approach might lead to non-physical effects as resonances in the J-V line (see, for example, Ref. [44]). Despite the danger of such spurious features showing up, we do not observe such effects in the investigated voltage range (50-150 kV/cm).

Measured laser spectra and calculated photon flux spectra for different voltage (current density) values are presented in Fig. 2.8.

For the calculated spectra, we used a level broadening of $\gamma_0 = 2.5$ meV and a carrier sheet density of $n_p = 2.5 \times 10^{11}$cm^{-2}. Both calculated and measured spectra show the same spectral position and the same broadening trend toward higher energies. The observed broadening is related to the increased population of upper laser levels with increased current. The observed blue-shift in the photon energy is related to the intersubband spacing increase between the upper laser states and the lower laser state character-

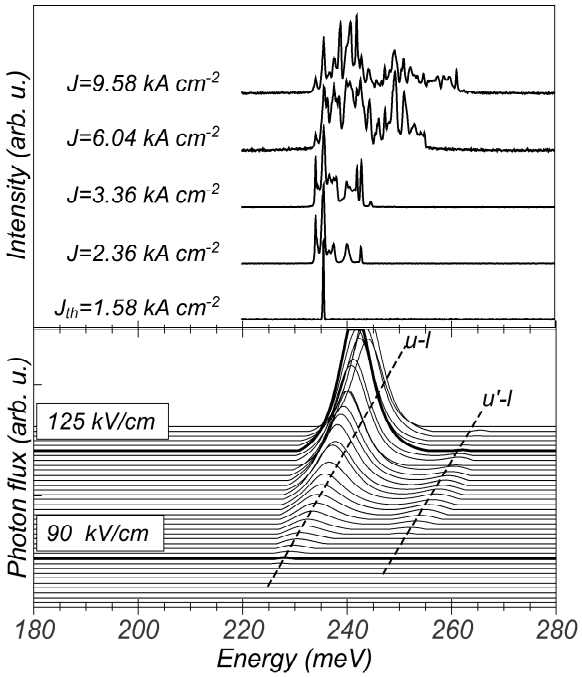

Figure 2.8: Emission spectrum for a 0.025×4.0 mm^2 device of the investigated QCL collected with a high-resolution Fourier-transform spectrometer. The heat sink temperature is 80 K, and the injected current density is varied as indicated. The corresponding calculated spectra as a function of voltage are shown in the lower panel with the broadening parameter $\gamma_0 = 2.5$ meV. Dashed lines indicate transitions between the upper laser levels u as well as u' and the lower laser level l. Thick solid lines denote the threshold voltage of 90 kV/cm and the voltage with maximum power emitting of 125 kV/cm.

istic for diagonal transition QCLs.

Compare with other model

This scattering-rate approach was applied for compare and description of electron scattering into upper levels in active region at low temperatures by Yuri Flores in last section of his Ph. D. thesis [69]. Fig. 2.9(b) shows the electron distribution calculated by phenomenological scattering rate model (solid circles) and by the leakage current method (open circles) for QCL active region which is presented in Fig. 2.9(a). This phenomenological model is applicable a low electron temperatures at low heat sink temperatures in contrast with the leakage current method where electron temperature is not frozen. Despite this small difference at low heat sink temperatures, both methods give same results

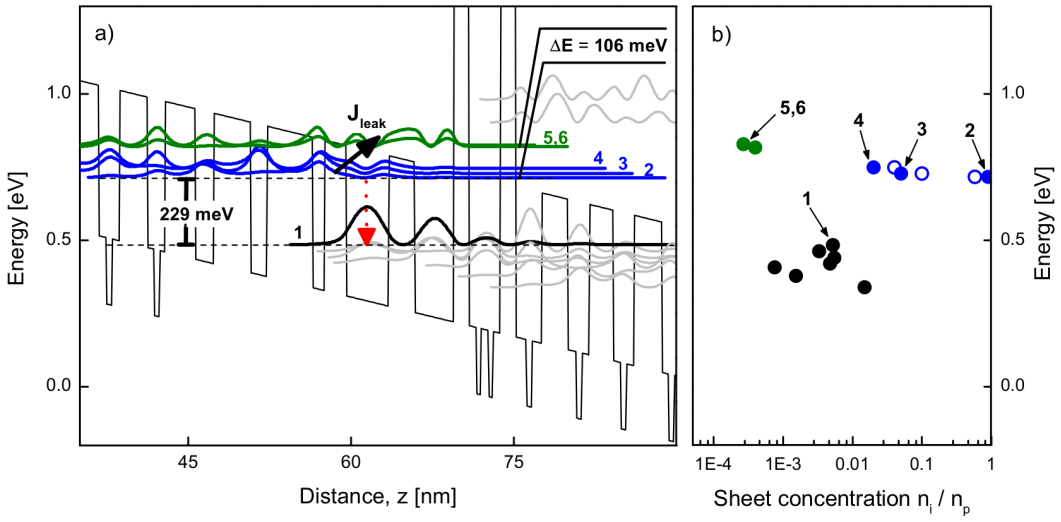

Figure 2.9: a) The conduction band profile of the investigated QCL for an applied electric field of 90 kV/cm at threshold with layer composition and thickness described in the original publication [36].
b) The right panel shows calculated by phenomenological scattering rate model the relative two-dimensional sheet densities n_i/n_p (the doping per period $n_p = 3.2 \times 10^{11}$ cm^{-2}) for a heat sink temperature of 80 K and an electron temperature of T_e = 130 K (solid circles). The open circles denote the sheet densities for the states $i = 2$, 3, and 4 as determined by fitting the leakage current for higher electron temperatures [69].

due to low scattering rate into upper levels.

2.2.4 Temperature dependent scattering-rate approach

In previous section we have shown that for mid-infrared QCLs, an empirical scattering-rate model based on the overlap integral may be preferred. Unfortunately, the scattering rate (Eq. 2.35) has a number of shortcomings:

- It is applicable for similar materials based on $In_{0.52}Al_{0.48}As/In_{0.53}Ga_{0.47}As$
- It works only at low temperature near 80 K, where phonons absorption is neglected.
- The interface roughness scattering rate is included through fitting parameter γ_0 for transitions between any levels.

For other cases empirical values will be different and approximation of them is indescribable. For more realistic model the various scattering mechanisms should be included separately.

In previous chapter we introduced transition rates $R_{i_{\mathbf{k}}j} \equiv R_{ij}(k)$ from initial state $|i\mathbf{k}>$ in the i^{th} level to j^{th} final level.

The average transition rate R^s_{ij} for a particular intersubband scattering mechanism s in QCLs can be written as [34]:

$$R^s_{ij} = \int_0^\infty dk\, kR^s_{ij}(k) f_i(k), \tag{2.38}$$

here $R^s_{ij}(k)$ is the transition rate by s-type scattering mechanism from a state with momentum k in the initial i-th subband to the states in the j-th subband, and $f_i(k)$ electron distribution.

The total transition rate of electron R_{ij} from the initial i-th subband to the j-th subband includes sum of different particular intersubband scattering mechanism s and optical transition rate $R^{opt}_{ij} = \int R^{opt}_{ij}(\omega)d\omega$ can be written as:

$$R_{ij} = \sum_s R^s_{ij} + R^{opt}_{ij}. \tag{2.39}$$

In the case of lightly doped semiconductors used in QCLs we have $(E_{ik} - E_i^F) >> k_B T_i$ and the Fermi-Dirac distribution approaches a classical Maxwell-Boltzmann distribution:

$$f_{MB} = \frac{\hbar^2}{m^* k_B T_e} \exp\left(-\frac{\hbar^2 k^2}{2m^* k_B T_e}\right), \tag{2.40}$$

where k_B, m^*, and T_e are the Boltzmann constant, effective electron mass, and temperature for electrons, respectively. Also this approach applicable for room temperature, where currently QCLs operate.

Generally different scattering models use empirical transition rates or transition rates between states of laser levels with complicated rate equation (*different modeling techniques for QCLs is observed in [34]*).

We will consider main scattering mechanism for QCLs and include separately them into Eq. 2.38 with Maxwell-Boltzmann distribution for electrons in the subbands.

Energy dependent scattering factor for interface roughness scattering.

In the first place the interface roughness scattering (IFR) will be considered because this scattering mechanism is included in the simplest form for previous phenomenological model. Also IFR has attracted attention in the last years and its effects on QCLs transport characteristics are being increasingly researched. Interface roughness scattering (IFR) is caused by the imperfections at the interface between the barrier and well material in the heterostructure, resulting in a local deviation of the interface $\Delta(x,y)$ from its average position. Normally the interface roughness is characterized by its standard deviation Δ and correlation length Λ. Following Ref. [34] the total transition rate from a given initial state $E_{i_\mathbf{k}}$ to any states of j^{th} level with energy E_j is giving by:

$$R_{ij}^{IFR}(k) = \frac{m^*}{\hbar^3}\Delta^2\Lambda^2 \sum_n V_{0n}^2(z)|\psi_i(z_n)\psi_j^*(z_n)|^2 \int_0^\pi d\phi \, \exp\left[-\frac{\Lambda^2 q^2(\phi)}{4}\right] \Theta(q(\phi)) = \tag{2.41}$$

$$\alpha_{IFR}\zeta'_{ij} \int_0^\pi d\phi \, \exp\left[-\frac{\Lambda^2 q^2(\phi)}{4}\right] \Theta(q(\phi))$$

with $q^2(\phi) = 2k^2 + q_0^2 - 2k\sqrt{k^2+q_0^2}\cos\phi$, $q_0^2 = 2m^*E_{ij}/\hbar^2$, $\alpha_{IFR} = \frac{m^*}{\hbar^3}\Delta^2\Lambda^2$, and $\zeta'_{ij} = \sum_n V_{0n}^2(z)|\psi_i(z_n)\psi_j^*(z_n)|^2$. Here $V_0(z_n)$ is the band offset and value of $\psi(z_n)$ are taken over all interfaces located at the position z_n. In case $E_i > E_j$, $q^2(\phi) > 0$ for all of k and ϕ, whereas if $E_i < E_j$, $q^2(\phi)$ is real only for all $k^2 > |q_0^2|$ and for all ϕ values. Under these conditions integration over $[0,\pi]$ by ϕ can be performed in Eq. (2.41) giving:

$$R_{ij}^{IFR}(k) = \pi\,\alpha_{IFR}\,\zeta'_{ij}\exp\left[-\frac{\Lambda^2(2k^2+q_0^2)}{4}\right]\,I_0\left(\frac{\Lambda^2}{2}k\sqrt{k^2+q_0^2}\right), \tag{2.42}$$

where $I_0(x)$ is the modified Bessel function of the first kind.

Inserting Eq. (2.42) into Eq. (2.38) the total rate for interface roughness scattering takes the form:

$$R_{ij}^{IFR} = \frac{\pi\hbar^2}{m^*k_BT_e}\,\alpha_{IFR}\,\zeta'_{ij}\int_0^\infty kdk\,\exp\left[-\frac{\hbar^2k^2}{2m^*k_BT_e} - \frac{\Lambda^2(2k^2+q_0^2)}{4}\right]\,I_0\left(\frac{\Lambda^2}{2}k\sqrt{k^2+q_0^2}\right). \tag{2.43}$$

In order to integrate Eq. (2.43) over all the interval $[0,+\infty)$ one has to take into account the asymptotical behavior of the $I_0(x)$ function:

$$I_0(x) = \frac{\exp(x)}{\sqrt{2\pi x}}\left[1+O\left(\frac{1}{x}\right)\right]\ \text{at}\ x\to\infty\ \text{and}\ I_0(x) = \sum_{k=0}^{\infty}\frac{(x^2/4)^k}{(k!)^2}. \tag{2.44}$$

In case of small x values in Eq. (2.44), Eq. (2.43) will be written as:

$$\begin{gathered} R_{ij}^{IFR} = \frac{\pi\hbar^2}{m^*k_BT_e}\,\alpha_{IFR}\,\zeta'_{ij}\exp\left(-\frac{\Lambda^2q_0^2}{4}\right)\times \\ \int_0^\infty kdk\,\exp\left[-\frac{\hbar^2k^2}{2m^*k_BT_e} - \frac{\Lambda^2k^2}{2}\right]\sum_{l=0}^{\infty}\frac{1}{(l!)^2}\left[\frac{\left(\frac{\Lambda^2}{2}k\sqrt{k^2+q_0^2}\right)^2}{4}\right]^l \end{gathered} \tag{2.45}$$

If $x < 1$, it is enough to retain only the terms with $k \le 1$ in sum of Eq. (2.45) for a very good approximation to the $I_0(x)$ function.

As a result the integration in Eq. (2.45) reduces to calculations of the integrals like:

$$\int_0^\infty \exp(-\mu y)\,dy = n!\mu^{-n-1},\ \text{where}\ \mu > 0. \tag{2.46}$$

Using Eq. (2.46), R_{ij}^{IFR} in Eq. (2.45) can be presented in explicit form:

$$\begin{gathered} R_{ij}^{IFR} = \frac{\pi\hbar^2}{m^* k_B T_e \beta}\, \alpha_{IFR}\, \zeta'_{ij} \exp\left(-\widetilde{\Lambda}^2 q_0^2\right) \Omega, \\ \text{with } \beta = \hbar^2 (2m^* k_B T_e)^{-1} + \Lambda^2/2,\ \widetilde{\Lambda} = \Lambda/2, \\ \text{and } \Omega = 1 + \tfrac{1}{\beta}\widetilde{\Lambda}^4 q_0^2 + \frac{\widetilde{\Lambda}^4}{2\beta}\left(1 + \frac{1}{4}\widetilde{\Lambda}^4 q_0^4\right) + \frac{1}{12\beta^3}\widetilde{\Lambda}^8 q_0^2 + \frac{1}{96\beta^4}\widetilde{\Lambda}^8. \end{gathered} \tag{2.47}$$

In case of $E_j > E_i$ the integration in Eq. (2.43) has to be performed from $|q_0|$ to ∞. That leads to zero contribution following the arguments above. Moreover, in the case of our calculation values, the Ω variable can be simplified to few first term of sum: $\Omega \approx 1 + \frac{1}{\beta}\widetilde{\Lambda}^4 q_0^2$.

Finally the transition rate for IFR can be written as:

$$R_{ij}^{IFR} = \rho^{IFR} \zeta'_{ij} \begin{cases} 1 & \text{for } E_{ij} \geq 0 \\ \exp\left(\dfrac{E_{ij}}{k_B T_e}\right) & \text{for } E_{ij} < 0 \end{cases}, \tag{2.48}$$

The Eq. (2.48) describes the transition rate for the interfaces roughness scattering mechanism from any i^{th} to j^{th} subbands in QCL structure for different temperatures. ρ^{IFR} depends from the energy between levels, the temperature, and the electron mass. In the opposite, the ζ'_{ij} depend from "overlap"$|\psi_i \psi_j|^2$ of i and j wave functions on the interfaces z_n with band offset V_0.

The accuracy of this approach for the $In_{0.52}Al_{0.48}As$-$In_{0.53}Ga_{0.47}As$ heterostructure at 80 K and 280 K is shown in Fig. 2.10, where line is described by Eq. (2.48). Open circles represent numerically integrated R_{ij}/ζ'_{ij} values by Eq. 2.43.

The temperature dependence of $\rho^{IFR}(E)$ is present in Fig. 2.11.

As we can see transition rate by IFR is approximately constant for energies more then 150 meV, which correspondent to transition from upper to lower laser levels. From another hand, the transition rate for energies near zero and fewer values is increased for high temperatures. This is correspond to depopulation of upper laser level into higher levels and electron "fit back" in the injector region.

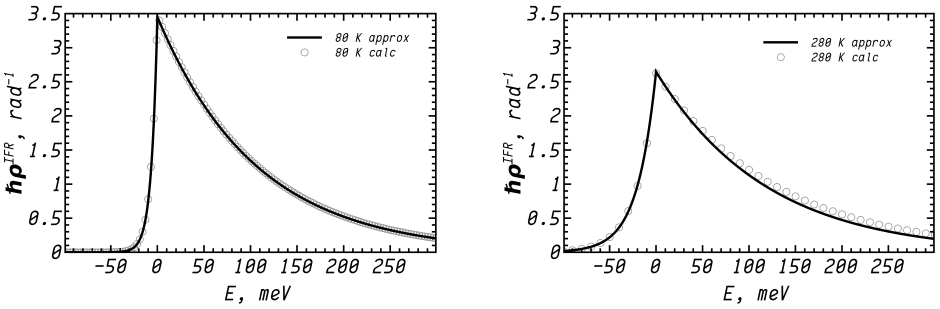

Figure 2.10: The energy factor $\rho^{IFR}(E)$ for IFR scattering multiplied by reduced Planck constant at 80 K (left) and 280 K (right) (black lines) with numerical calculations as open circles.

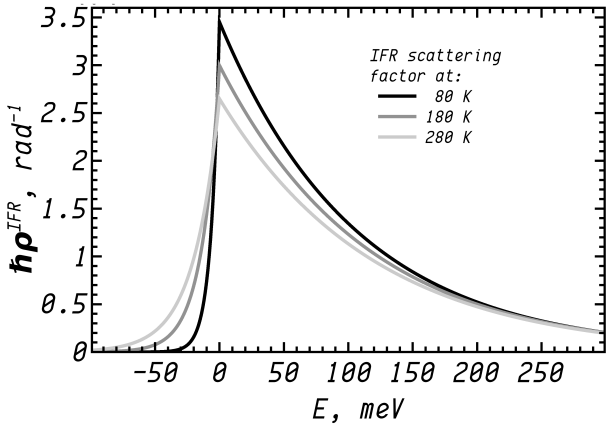

Figure 2.11: The energy factor $\rho^{IFR}(E)$ for IFR scattering at 80 K (black line), 180 K (gray line), and 280 K (light gray line).

Energy dependent scattering factor for longitudinal optical phonons.

The next but the main scattering mechanism in QCLs is due to longitudinal optical (LO) phonons. According to Ref. [33], for the scattering by longitudinal optical phonons the $R^s_{ij}(k)$ function has form (Eq. (1.17)):

$$R^{LO}_{ij}(k) = \alpha_{LO} \int_0^\infty dK_z \, F_1(k, K_z) \left| G_{ij}(K_z) \right|^2, \tag{2.49}$$

where

$$F_1(k,K_z)=\Theta\left(k^2+\frac{2m^*\Delta_{ij}}{\hbar^2}\right)\left[K_z^4+2K_z^2\left(2k^2+\frac{2m^*\Delta_{ij}}{\hbar^2}+\left(\frac{2m^*\Delta_{ij}}{\hbar^2}\right)^2\right)\right]^{-\frac{1}{2}}, \quad (2.50)$$

and the form factor for K_z phonon wave vector is defined as $G_{ij}=\int_{-\infty}^{+\infty}dz\,\Psi_j^*(z)\exp(-iK_z z)\Psi_i(z)$. α_{LO} is $\frac{m^*e^2\omega_{LO}}{2\pi\hbar^2}(\varepsilon_\infty^{-1}-\varepsilon_s^{-1})(N_{LO}+\frac{1}{2}\pm\frac{1}{2})$ and $\Delta_{ij}^{LO}=E_i-E_j\mp E_{LO}$ with sign "-" for emission and sign "+" for absorption processes, respectively. The LO phonon branch $E_{LO}(\omega)$ is considered as dispersionless, $E_{LO}(\omega)=E_{LO}\sim\hbar\omega_{LO}$. ε_∞ and ε_s are the high- and low-frequency permittivities of semiconductor, respectively. $N_{LO}=[\exp(\hbar\omega_{LO}/k_BT_l)-1]^{-1}$ is the LO-phonon occupation number in the emission (sign "+") and absorption (sign "-") processes.

Inserting Eq. (2.49) into Eq. (2.38) one gets:

$$R_{ij}^{LO}=\alpha_{LO}\cdot\int_0^\infty dK_z\,\left|G_{ij}(K_z)\right|^2\left(\int_0^\infty dk\,kF_1(k,K_z)f_{MB}(k)\right)= \quad (2.51)$$

$$\alpha_{LO}\cdot\int_0^\infty dK_z\,\left|G_{ij}(K_z)\right|^2 Q_{ij}(K_z),$$

where

$$Q_{ij}(K_z)=\int_0^\infty dk\,kF_1(k,K_z)f_{MB}(k). \quad (2.52)$$

After integration over k in Eq. 2.52 function $Q_{ij}(K_z)$ turns to:

$$Q_{ij}(K_z)=\frac{\sqrt{\pi\mu}}{2K_z}\exp(\alpha)\begin{cases}\operatorname{erfc}\left(\sqrt{\alpha}\right) & \text{for } \Delta_{ij}^{LO}\geq 0\\ \operatorname{erfc}\left(\sqrt{\alpha-\mu\beta}\right) & \text{for } \Delta_{ij}^{LO}<0\end{cases}, \quad (2.53)$$

with $\mu=\hbar^2/2m^*k_BT_e$, $\beta=2m^*\Delta_{ij}^{LO}/\hbar^2$, and $\alpha=\mu\left[\left(K_z^2+\beta\right)/2K_z\right]^2$.

The complementary error function $erfc(x)$ has an asymptotic representation for large values of x:

$$\operatorname{erfc}(x)\approx\frac{e^{-x^2}}{x\sqrt{\pi}}\sum_{k=0}^{\infty}\frac{(-1)^k(2k-1)!}{(2x^2)^k}. \quad (2.54)$$

The asymptotic series in Eq. 2.54 is not convergent, however, for large x the function

$erfc(x)$ can be substantially well approximated already by a few first terms of the series, say:

$$\mathrm{erfc}(x) \approx \frac{e^{-x^2}}{x\sqrt{\pi}}\left(1-\frac{1}{2x^2}\right). \tag{2.55}$$

Taking this into account we find that in case of large values of K_z, when $K_z \gg |\beta|$ and $\alpha \to \mu K_z^2/4$,

$$Q_{ij}(K_z) \to \frac{1}{K_z^2}. \tag{2.56}$$

Thus the integrand in Eq. 2.51 is a product of two rapidly decaying functions, $\left|G_{ij}(K_z)\right|^2$ and $Q_{ij}(K_z)$, if $K_z \to \infty$. Turning back to calculation of transition rate R_{ij}^{LO} let's split into two parts the interval of integration:

$$R_{ij}^{LO} = \alpha_{LO} \lim_{K_z^{lim}\to\infty}\left[\int_0^{K_z^{lim}} dK_z \ \left|G_{ij}(K_z)\right|^2 Q_{ij}(K_z) + \int_{K_z^{lim}}^{\infty} dK_z \ \left|G_{ij}(K_z)\right|^2 Q_{ij}(K_z)\right]. \tag{2.57}$$

The second term in Eq. (2.57) tends zero, where as for calculation of first term we apply the first mean value theorem for definite integrals. While the function $Q_{ij}(K_z)$ is continuous on the interval $[0, K_z^{lim}]$ and the function $|G_{ij}(K_z)|^2$ is an integrable function that does not change sign on the same interval, then there exists point $\overline{K_z}$ in the interval $[0, K_z^{lim}]$ such that:

$$\begin{gathered} R_{ij}^{LO} = \alpha_{LO} \ \lim_{K_z^{lim}\to\infty}\left[\int_0^{K_z^{lim}} dK_z \ \left|G_{ij}(K_z)\right|^2 Q_{ij}(K_z)\right] = \\ \alpha_{LO} \ \lim_{K_z^{lim}\to\infty} Q_{ij}(\overline{K_z}) \int_0^{K_z^{lim}} dK_z \ \left|G_{ij}(K_z)\right|^2. \end{gathered} \tag{2.58}$$

For the large value of K_z^{lim} the $\overline{K_z} \to$ const and Eq. 2.58 takes the form:

$$\begin{gathered} R_{ij}^{LO} = \alpha_{LO} \ \lim_{K_z^{lim}\to\infty} Q_{ij}(\overline{K_z}) \int_0^{K_z^{lim}} dK_z \ \left|G_{ij}(K_z)\right|^2 = \\ \alpha_{LO} \ Q_{ij}(\overline{K}_{lim}) \int_0^{\infty} dK_z \ \left|G_{ij}(K_z)\right|^2. \end{gathered} \tag{2.59}$$

This equation can be written in terms of integral of overlapping for electron wavefunc-

tions ζ_{ij}:

$$R_{ij}^{LO} = \alpha_{LO}\, Q_{ij}(\overline{K}_{lim}) \int_0^\infty dK_z \, \left|G_{ij}(K_z)\right|^2 = \pi\alpha_{LO}\, Q_{ij} \int_{-\infty}^{\infty} dz \, \left|\psi_j(z)\right|^2 |\psi_i(z)|^2 = \pi\alpha_{LO}\, Q_{ij}\zeta_{ij}. \tag{2.60}$$

This equation can be rewritten in terms of energies:

$$R_{ij}^{LO}(E_{ij}) = \frac{\sqrt{\pi}e^2P}{8\hbar}\frac{E_{LO}}{\sqrt{E_z k_B T_e}}\zeta_{ij}\exp\left[a_{LO}\right] \cdot \begin{cases} \mathrm{efrc}\left(\sqrt{a_{LO}}\right) & \text{for } \Delta_{ij}^{LO} > 0 \\ \mathrm{efrc}\left(\sqrt{b_{LO}}\right) & \text{for } \Delta_{ij}^{LO} \le 0 \end{cases} \tag{2.61}$$

$$\text{with } E_z = \tfrac{K_z^2\hbar^2}{2m^*},\ a_{LO} = \frac{(E_z+\Delta_{ij}^{LO})^2}{4E_z k_B T_e},\ \text{and}\ \ b_{LO} = a_{LO} - \frac{\Delta_{ij}^{LO}}{k_B T_e} = \frac{(E_z-\Delta_{ij}^{LO})^2}{4E_z k_B T_e}.$$

On this moment only value of fitting energy $E_z = K_z^2\hbar^2/2m^*$ is undefined. This value can be extracted from method applied for previous compact model. The values of $\rho^{LO} = R_{ij}^{LO}/\zeta_{ij}$ are calculated for few typical QCL designs taken from literature. The transition rates by LO-phonon were found by numerical integration over K_z and k in Eq. (2.51). The overlap $\zeta_{ij} = \int dz\ \psi_i^2(z)\psi_j^2(z)$ of wave functions and energy E_{ij} are taken from solution of Schrödinger equation applied for given designs.

Fig. 2.12 shows the calculated data for 80 K, 180 K, and 280 K as open circles and squares for LO-phonon emitting and absorption processes, respectively. According to low probability of LO-phonon absorption($\rho^{LO-} \sim 0$), these values on Figure are missed at 80 K. The respective results for Eq. (2.61) are shown in Fig. 2.12 for the fit parameter $E_z = 0.4 \cdot E_{LO}$ as a black solid lines.

Finally the transition rate due to LO-phonons can be written as:

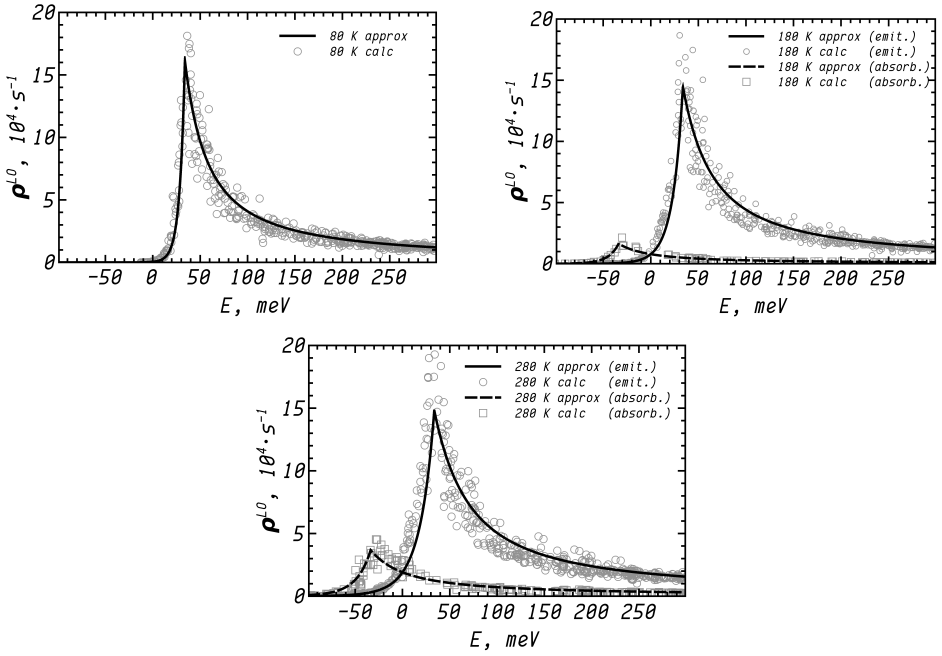

Figure 2.12: The values of energy factor $\rho^{LO}(E)$ for LO-phonon scattering at 80, 180, 280 K temperatures. Open symbols denote approximate values R_{ij}/ζ_{ij} of LO-phonon emission and absorption processes as circles and squares, respectively. Black solid lines are the fit data of ρ_{ij}^{LO} with $E_z = 0.4 \cdot E_{LO}$.

$$R_{ij}^{LO}(E_{ij}) = \rho^{LO}\zeta_{ij},$$

$$\text{with } \rho^{LO} = \frac{\sqrt{\pi}e^2P}{8\hbar}\sqrt{\frac{E_{LO}}{0.4k_BT_e}}\exp[a_{LO}] \cdot \begin{cases} \text{efrc}\left(\sqrt{a_{LO}}\right) & \text{for } \Delta_{ij}^{LO} > 0 \\ \text{efrc}\left(\sqrt{b_{LO}}\right) & \text{for } \Delta_{ij}^{LO} \le 0 \end{cases} \tag{2.62}$$

$$E_z = 0.4 \cdot E_{LO},\ P = (\varepsilon_\infty^{-1} - \varepsilon_s^{-1})(N_{LO} + \tfrac{1}{2} \pm \tfrac{1}{2}),\ N_{LO} = \left[\exp\left(\frac{\hbar\omega_{LO}}{k_BT_l}\right) - 1\right]^{-1}$$

$$a_{LO} = \frac{(E_z + \Delta_{ij}^{LO})^2}{4E_zk_BT_e},\ \text{and}\ \ b_{LO} = \frac{(E_z - \Delta_{ij}^{LO})^2}{4E_zk_BT_e},\ \Delta_{ij}^{LO} = E_{ij} \mp E_{LO}.$$

Moreover, the scattering rates can be calculated for both emitting and absorption of LO-phonon processes. Fig. 2.13(a) shows the energy dependent factors for transition rate by LO-phonon emission ρ^{LO+} and absorption ρ^{LO-} processes at 280 K, respectively. Additionally, summarized energy factor $(\rho^{LO+} + \rho^{LO-})$ is shown in Fig. 2.13(a) by black

solid line.

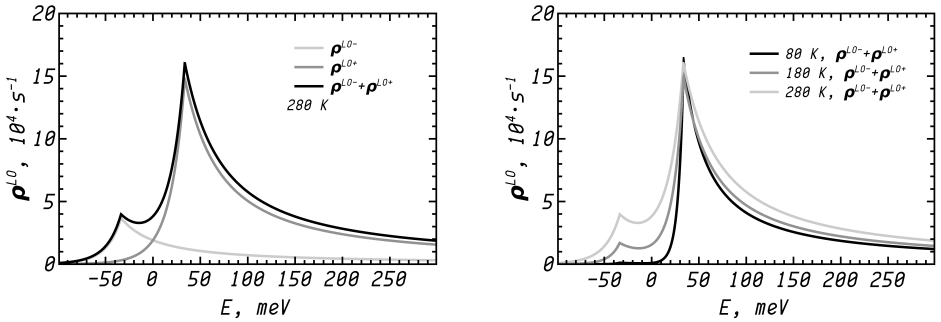

Figure 2.13: a) The energy dependent factor $\rho^{LO+}(E)$, $\rho^{LO-}(E)$, and $\rho^{LO+}(E)+\rho^{LO-}(E)$ for LO-phonon emission, absorption, and both processes at 280 K.
b) The summarized energy factor $\rho^{LO+}+\rho^{LO-}$ due to LO-phonons at 80 K, 180 K, and 280 K temperatures.

Fig. 2.13(b) shows the summarized energy factor $\rho^{LO+}+\rho^{LO-}$ for electron-LO-phonon interaction at different temperatures. Providing that overlap ζ_{ij} is approximately constant for various temperatures, the transition rate $R_{ij}^{LO}(E_{LO})$ at LO-phonon resonance energy E_{LO} doesn't depend on temperature more then 80 K. In contrast to transition rate at E_{LO}, $R_{ji}^{LO}(-E_{LO})$ rate increases with increasing temperature according to number of LO-phonons N_0 in Eq. (2.62). The last statement is executed until room temperatures while $\rho^{LO+}(-E_{LO})\approx 0$ with respect to $\rho^{LO-}(-E_{LO})$. Moreover, in this region of temperatures, the transition rate for energies over 200 meV is approximately irrespective of temperature. According to previous assumption, the three level laser system with upper level '3' will have temperature decreasing of depopulation for lower laser level '2' by additional scattering from lowest laser level '1'.

According to data from Fig. 2.13(b), the summarized energy factor ρ^{LO} for LO-phonon scattering for energy diapason of $0-E_{LO}$ increases with temperature increasing. This condition is good for "bound-to-continuum" designs, where energies between lower laser levels less than E_{LO}. In this case the depopulation of lower laser level will be more stable in temperature.

Energy dependent scattering factor for acoustic phonons.

The acoustic phonon scattering doesn't play important role in scattering processes for the cascade structures such as quantum cascade lasers. But more important to include the maximum number of possible scatterings for QCLs for realistic simulation of processes in devices.

For calculation of the acoustic phonon scattering rate we take into account that the energy of acoustic phonons ω_A are usually significantly smaller than the typical intersubband separations $\Delta E_{ij} = E_i - E_j$ which can be of several hundred *meV* by value. Besides an acoustic phonon branch can be approximated by a linear function of phonon wave vector module K, $\omega_A = v_s K$, where v_s is a velocity of a sound wave. In this case the transition rate R_{ij}^A for acoustic phonon scattering according to Eq. (2.38) can be written as:

$$R_{ij}^A = \int_0^\infty dk\, k R_{ij}^A(k) f_{MB}(k), \tag{2.63}$$

here $R_{ij}^A(k)$ defines the rate for the electron from a state with momentum k in the initial i-th subband to transit into all states in the j-th subband with participation of acoustic phonons. Following Ref. [33] the $R_{ij}^A(k)$ function can be calculated using the expression:

$$R_{ij}^A = \frac{D_A^2}{2\rho_c v_s (2\pi)^2} \iint \left(N_A + \frac{1}{2} \pm \frac{1}{2} \right) K \delta\left(E_{jk_j} - E_{ik_i} \mp \hbar\omega_A \right) dK_z d\overrightarrow{K}_{xy}, \tag{2.64}$$

where D_A is an acoustic deformation potential, ρ_c is the crystal density, N_A is a phonon occupation number of a mode with wave vector $\overrightarrow{K}$:

$$N_A = \left[\exp\left(\frac{\hbar\omega_A}{k_B T} \right) - 1 \right]^{-1}. \tag{2.65}$$

$\overrightarrow{K_{xy}}$ and K_z are in-plane and perpendicular components of phonon wave vector;

$$E_{ik_i} = E_i + \frac{\hbar^2 k_i^2}{2m^*} \text{ and } E_{jk_j} = E_j + \frac{\hbar^2 k_j^2}{2m^*}. \tag{2.66}$$

Let us take into account that for all but the lowest temperatures equation (2.65) can be approximate with:

$$N_A \approx N_A + 1 \approx \frac{k_B T}{\hbar v_s K}, \tag{2.67}$$

and that due to inequality $\hbar\omega_A \ll E_{ij}$ the phonon energy can be put zero in Eq. (2.64) (the quasi-elastic approximation). In this case introducing the polar coordinates for the in-plane phonon vector $\overrightarrow{K}_{xy}$, equation (2.64) can be reduced to the form as follows:

$$R_{ij}^A(k) = \frac{k_B T m^* D_A^2}{\rho_c v_s (2\pi)^2 \hbar^3} \iint_0^{2\pi} \left|G_{ij}(K_z)\right|^2 \delta\left(K_{xy}^2 + 2k_i K_{xy}\cos\varphi + \frac{2m^* E_{ij}}{\hbar^2}\right) K_{xy} dK_{xy} d\varphi dK_z. \tag{2.68}$$

Performing integration over K_z and K_{xy} in Eq. (2.68) one gets:

$$R_{ij}^A(k) = 2\pi\alpha_A \zeta_{ij} \int_0^{2\pi} d\varphi \, \frac{\Theta(v_1)v_1 + \Theta(v_2)v_2}{v_2 - v_1}, \tag{2.69}$$

with

$$v_{1,2} = -k\cos\varphi \pm \sqrt{(k\cos\varphi)^2 - \frac{2m^* E_{ij}}{\hbar^2}} \text{ and } \alpha_A = \frac{k_b T m^* D_a^2}{\rho_c v_s^2 (2\pi)^2 \hbar^3}. \tag{2.70}$$

As can be seen due to step functions, v_1 and v_2 in the numerator of Eq. (2.69) have to be positive and $v_1 > v_2$. If $E_{ij} < 0$, $v_2 < 0$ and Eq. (2.69) reduces to:

$$\begin{aligned} R_{ij}^A(k) &= 2\pi\alpha_A \zeta_{ij} \int_0^{2\pi} d\varphi \left[\frac{-k\cos\varphi + \sqrt{(k\cos\varphi)^2 - \frac{2m^* E_{ij}}{\hbar^2}}}{2\sqrt{(k\cos\varphi)^2 - \frac{2m^* \Delta E_{ij}}{\hbar^2}}}\right] \\ R_{ij}^A(k) &= 2\pi\alpha_A \zeta_{ij} \int_0^{2\pi} d\varphi \left[\frac{-k\cos\varphi}{2\sqrt{(k\cos\varphi)^2 - \frac{2m^* E_{ij}}{\hbar^2}}} + \frac{1}{2}\right] \end{aligned} \tag{2.71}$$

If $E_{ij} > 0$, v_1 and v_2 can be positive only in case of $\cos\varphi < 0$ and $R_{ij}^A(k)$ takes the form:

$$R_{ij}^{A}(k) = 2\pi\alpha_A\zeta_{ij}\int_{\pi/2}^{3\pi/2} d\varphi\,\frac{v_1+v_2}{v_1-v_2} = 2\pi\alpha_A\zeta_{ij}\int_{\pi/2}^{3\pi/2} d\varphi\,\frac{-k\cos\varphi}{2\sqrt{(k\cos\varphi)^2-\frac{2m^*E_{ij}}{\hbar^2}}}. \quad (2.72)$$

Introducing new variable $y = \sin\varphi$ the integrand can presented in form:

$$R_{ij}^{A}(k) = 2\pi\alpha_A\zeta_{ij}\int_{-1}^{1}\frac{dy}{\sqrt{a-y^2}} = 2\pi\alpha_A\zeta_{ij}\int_{-\sqrt{a}}^{\sqrt{a}}\frac{dy}{\sqrt{a-y^2}} = \quad (2.73)$$

$$2\pi\alpha_A\zeta_{ij}\arcsin\tfrac{y}{\sqrt{a}}\Big|_{-\sqrt{a}}^{\sqrt{a}} = 2\pi^2\alpha_A\zeta_{ij}.$$

with $a = \left(1-\dfrac{2m^*E_{ij}}{\hbar^2k^2}\right)$

It follows from Eq. (2.71) and (2.73) that $R_{ij}^{A}(k)$ is zero if $E_j > E_{ik}$ in the quasi elastic approximation and $R_{ij}^{A} = 2\pi^2\alpha_A\zeta_{ij}$ otherwise. Inserting these results in Eq. (2.63) and integrating over k we get:

$$R_{ij}^{A} = \frac{m^*k_BT_lD_a^2}{2\rho_c v_s^2\hbar^3}\zeta ij\begin{cases} 1 & \text{for } E_{ij}\geq 0 \\ \exp\left(\dfrac{E_{ij}}{k_BT_e}\right) & \text{for } E_{ij}<0 \end{cases}, \quad (2.74)$$

that coincides with results Jirauschek *et al* if both emission and absorption will be included by an additional factor of 2.

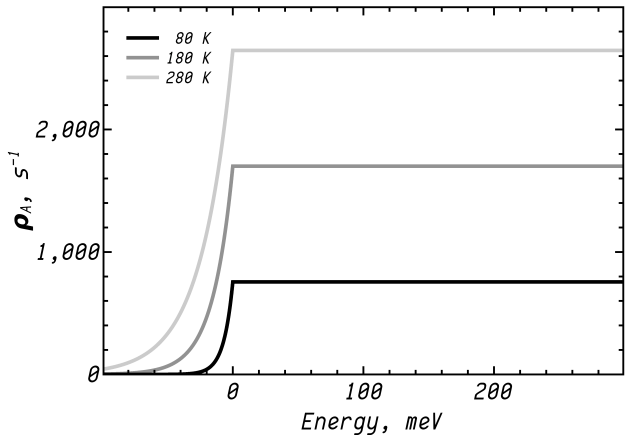

Figure 2.14: The energy dependent factor $\rho^A(E)$ for both acoustic phonon emission and absorption processes at 80 K, 180 K, and 280 K.

2.2.5 T_0 from temperature dependent scattering model

The most important characteristics for the QCLs are threshold current I_{th}, slope efficiency $\frac{dP}{dI}$, and peak power P_{max}. These characteristics can be defined from the power-voltage-current measurements. Moreover, these parameters depend on temperature for typical semiconductor lasers. The threshold current density is increased with increasing heat sink temperature of QCL following empirical dependence:

$$J_{th}(T) = J_0 \exp\left(\frac{T}{T_0}\right), \tag{2.75}$$

where T_0 is so-called characteristic temperature, which typically is used in the temperature range from 150 K to RT and above for different active region designs. Often in this equation the term J_1 is added in order to expand the range up to low temperatures. Furthermore, this term J_1 is applicable when leakage current can't be neglected.

Generally, the characteristic temperature T_0 depends not only from the type of active region design. Typically the effect of this characteristic is defined by geometric and optical properties of resonator. In turn a purity of materials, shape, length, and width of resonator influence on a wave guide and mirror losses, and optical confinement factor. The electron concentration per period has influences the electro-optical characteristics also.

The gain-current density characteristic can be used for calculation of J_{th} value, when gain and losses are equal in resonator: $g\Gamma = \alpha$. Following temperature-dependent model, the threshold current $J_{th}(T)$ can be extracted for different temperatures with subsequent calculation of T_0 value for comparison or prediction of QCL behavior. Usually the experimental data are measured or specified with some accuracy. For example, the electron sheet density in QCL devices has accuracy $n_e \pm 0.1 n_e$ from one growth to another.

According to Eq. 2.16 the current density J is proportional to the electron sheet density per period n_e. In relative units J/n_e, the current density j created by one electron can be written as:

$$j = \frac{J}{n_e} = \sum_{i,j=1}^{N} n_i^0 [\phi_{ij} R_{ij} - R_{i,j+N} + R_{i,j-N}], \tag{2.76}$$

where n_i^0 denotes relative electron sheet density for i-level with condition $\sum_i n_i^0 = n_e^{-1} \sum_i n_i = 1$.

In the same way, the gain produced by one electron g/n_e can be written following to Eq. 2.21:

$$\eta(\omega) = \frac{g(\omega)}{n_e} = \frac{\pi e^2 \omega}{c\varepsilon_0 n_{eff} L_p} \sum_{ij}^{E_i > E_j} (n_i^0 - n_j^0) |Z_{ij}|^2 L_{ij}(\omega), \tag{2.77}$$

The once calculation of gain versus current density in relative units allows to fit numerical data with experimental threshold current density J_{th}. This method allows to evaluate one characteristic, for example, current density J_{th} when other characteristics such as the electron sheet density per period and losses are defined. It is applicable for the lightly doped heterostructures where variation of electron concentration do not affect to transition rates.

We applied the temperature dependent scattering-rate model for calculation of relative gain-current density characteristics. The QCL active region under investigation is presented in Fig. 2.15 and is similar to published in Ref. [39].

Fig. 2.16 shows fitted relative maximum gain – current density $\eta(j)$ characteristics for temperature range 100-380 K with 20 K step. The best fitted $\eta(j,T)$ are taken for the calculation of T_0 characterization temperature which also is obtained from measurements. Furthermore, the relevant loss $a/\Gamma = \frac{\alpha_w + \alpha_w}{n_e \Gamma}$ is shown in Fig. 2.16. The intersection points of relevant gain η and relevant loss a/Γ correspond to relevant threshold current density j_{th} at different temperatures. The calculation of T_0 is possible with received $j_{th}(T)$ for different temperatures.

The measured T_0 characteristics and results discusion are published in Ref. [70]. We will consider results for the current pulse mode, where heat sink and effective active region temperatures can be approximately equivalent.

The 10-period strain compensated InGaAs-InAlAs structure was grown on a low doped

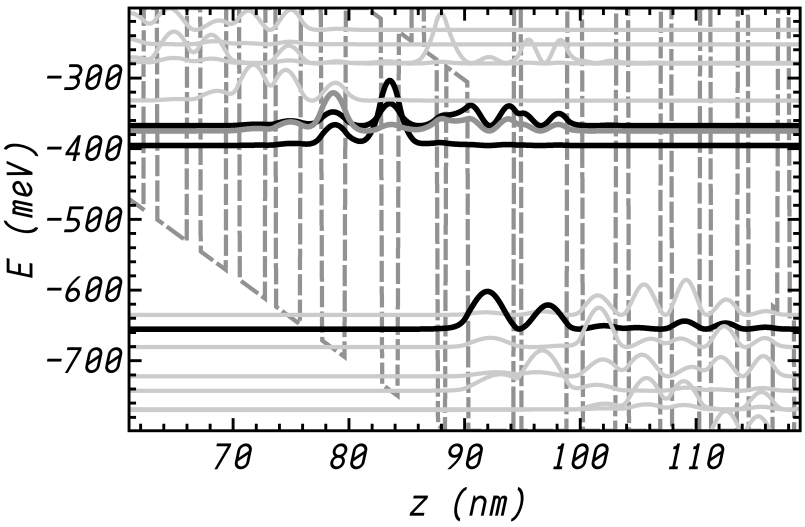

Figure 2.15: Conduction band profile and moduli-square of the Wannier-Stark states of a single cascade under 117 kV/cm bias. The upper and lower laser states are in solid black lines, respectively. The ground states are in black, and the excited states are in gray.The layer thickness in nm: 1.1/*1.55*/1.2/**0.9**/1.2/*0.7*/2.0/*4.0*/**0.6**/*3.9*/**1.4**/*2.9*/**1.1**/*2.7*/**1.0**/*2.4*/**1.0**/*2.3*/**0.9**/*2.1*/0.5/**0.9**/0.5/*1.95*/1.1/**0.9**, where the $In_{0.52}Al_{0.48}As$ layers are denoted by regular, the $In_{0.73}Ga_{0.27}As$ layers by italic, the **AlAs** layers by bold fonts.

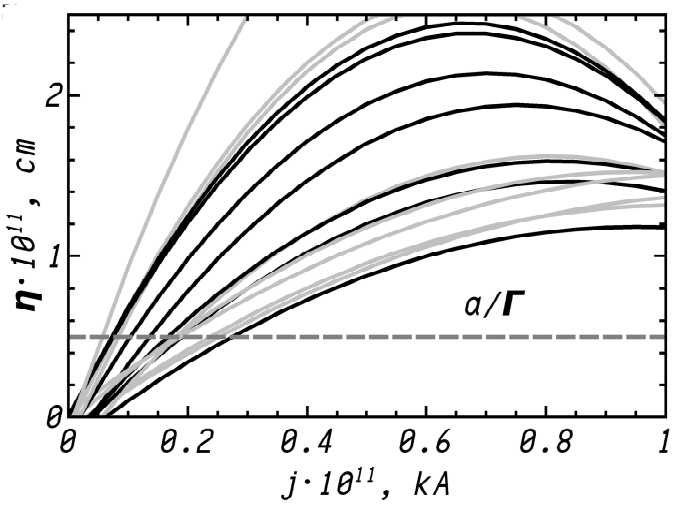

Figure 2.16: The relative gain η vs. current density j per one electron at different temperatures in range 100-380 K (20 K step). Black solid lines denote best fitted curves taken for T_0 characterization (120, 140, 200, 260, 280, 320, and 380 K). The relative loss a/Γ is in dashed line.

InP:S substrate using gas-source molecular beam epitaxy with expected electron sheet density per cascade 4×10^{11} cm^{-2}. The grown structure was processed into 30 μm wide ridges. The resonator with 0.4×30 μm^2 facets approximately has optical confinement factor about $\Gamma = 0.3$. Here, two different laser stripes are tested. One of them is 2-mm-long 2-side HR-coated test-stripe with $T_0 = 143$ K. In this case $\alpha \approx \alpha_w$ losses are defined to 2 cm^{-1}. Another one is 4 mm long ridge with one-side HR-coated facet with losses $\alpha = \alpha_w + \alpha_m$ equal to 3.5 cm^{-1} and characteristic temperature $T_0 = 160$ K.

With writing system equation:

$$\frac{\alpha}{\Gamma} = n_e \cdot \eta(j_{th}, T) \;\Leftrightarrow\; J_{th}(T) = n_e \cdot j_{th}(\eta, T) \tag{2.78}$$

and substituting the real electron sheet density n_e and losses α, the threshold current density $J_{th}(T)$ can be calculated for different temperatures T. Fig. 2.17 shows received T_0 characteristic temperature, approximated from $J_{th}(T) = J_0 \exp(T/T_0)$, as a function of total losses α for different electron sheet densities n_e.

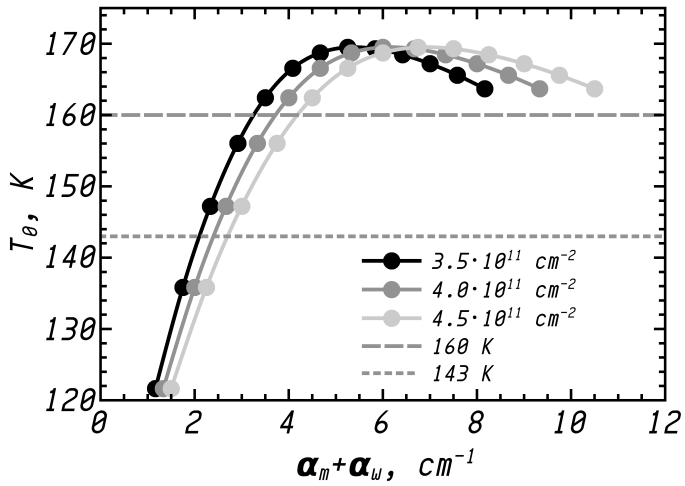

Figure 2.17: Calculated characteristic temperatures T_0 as a function of total losses for 3.5, 4.0, and 3.5×10^{11} cm^{-2} electron sheet density per one period denote black, gray, and light gray solid lines with circles, respectively. T_0 of 143 K and 160 K equal to experimental data are in short and normal dashed lines, respectively.

The value of 3.5×10^{11} cm^{-2} is defined as best-fitted electron sheet density for experi-

mental data (T_0, α) equals to (143 K, 2 cm^{-1}) and (160 K, 3.5 cm^{-1}), respectively.

Additionally, the characteristic temperatures T_0 are calculated as a function of total losses for 3.5×10^{11} cm^{-2} electron sheet density per one cascade for optical confinement factors values $\Gamma = 0.25$, 0.30, and 0.35. Fig. 2.18 shows these dependencies.

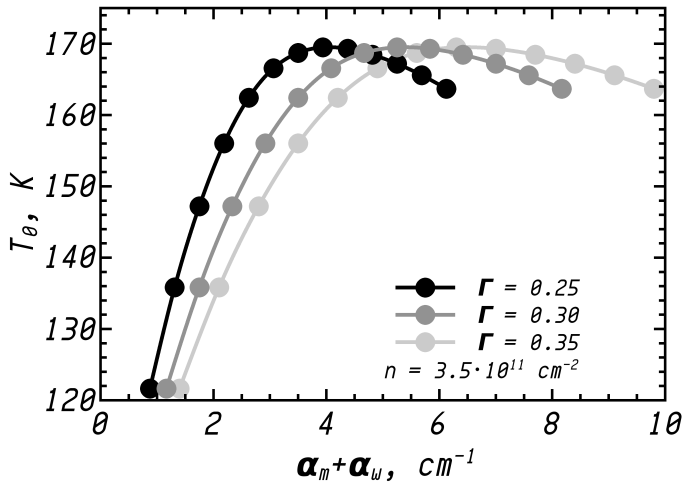

Figure 2.18: Calculated characteristic temperatures T_0 as a function of total losses for optical confinement factor of 0.25, 0.30, and 0.35 values denote black, gray, and light gray solid lines, respectively. The electron sheet density per one period is 3.5×10^{11} cm^{-2}.

Obtained results show influences of cavity geometry though α_m, α_w, and Γ to temperature dependence of threshold current density by T_0 characteristic temperature. In this approach losses is taken as independent from temperature.

2.2.6 Temperature dependence of optical gain and losses

Optical gain and waveguide loss are important characteristics for the describing QCL performances, such as threshold current, optical slope efficiency, maximum power. Mirror losses are not considered due to possibility to control it through HR-coating.

For the measuring gain coefficient g_d and waveguide loss α_w in QCL devices the $\frac{1}{L}$-method is the most applicable. This method is based on measuring threshold current density J_{th} for several stripes with different length L, which have mirror losses $\alpha_m = -ln(R)/L$ inversely proportional to cavity length L:

$$J_{th}(T) = \frac{\alpha_w(T)}{g_d(T)\Gamma} - \frac{ln(R)}{g_d(T)\Gamma}\frac{1}{L}. \tag{2.79}$$

Here optical confinement factor Γ and mirror reflectivity on facets $R = \frac{n_{eff}-1}{n_{eff}+1}$ with reflective index n_{eff} are independent from temperature. Other dependencies ($\alpha_w(T)$ and $g_d\Gamma$) can be extracted from measured threshold current density for different cavity lengths and temperatures.

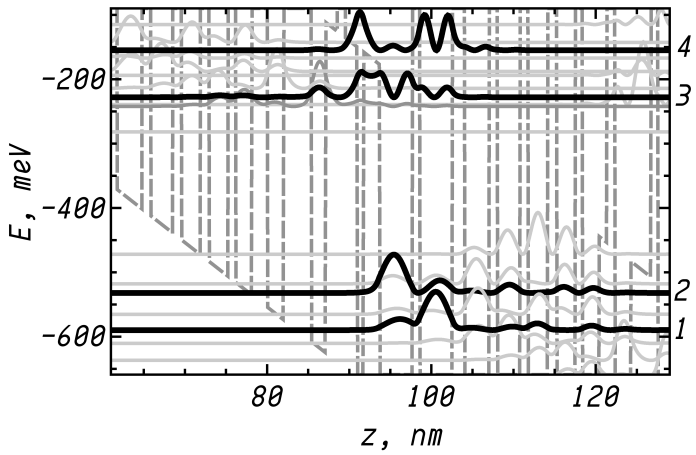

Figure 2.19: Conduction band profile and moduli-square of the Wannier-Stark states of a single cascade under 100 kV/cm bias. The upper and lower laser states are in green and blue lines, respectively. The ground states are in black, and the excited states are in gray.The layer thickness in nm: **0.9**/*1.7*/1.5/**0.9**/1.5/*0.7*/2.0/*4.0*/**0.9**/*4.0*/**1.4**/*3.1*/**1.0**/*2.7*/**1.0**/*2.4*/**1.0**/*2.3*/**0.9**/*2.0*/1.0/**0.9**/*1.9*/2.5, where the $In_{0.52}Al_{0.48}As$ layers are denoted by regular, the $In_{0.73}Ga_{0.27}As$ layers by italic, the **AlAs** layers by bold fonts.

The active region of investigated QCL is present in Fig. 2.19 and similar to observed in previous section. The power-current density characteristics were received for 0.9, 1.8, and 3.6 mm cavity stripes in temperature range 60-280 K with 10 K step. Fig. 2.20 shows $P-J$ characteristics near threshold for 3.6 mm stripe. Received $J_{th}(T)$ for measured samples are present in Fig. 2.21(a). For measured temperature dependent threshold current densities $J_{th}(T)$, the optical gain $g_d(T)\Gamma$ and waveguide losses $\alpha_w(T)$ were fitted by Eq. 2.79. The received characteristics are shown in Fig. 2.21(b).

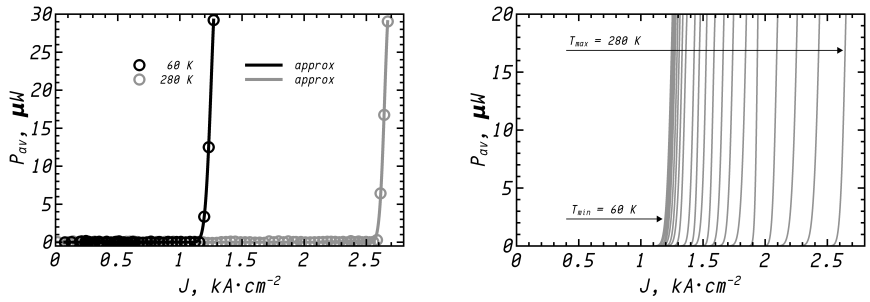

Figure 2.20: Power-current density characteristic for QCL devices with 3.6 mm length at 60 and 280 K are in black and gray color, respectively. Open circles denote measured point, fitted curves are by solid lines.
b) Fitted power-current density characteristic for QCL devices at temperature range 60-280 K. Arrows show first and last $P-J$ curves for 60 and 280 K, respectively. Curves measured with step 10 K and accuracy $\pm$0.5 K

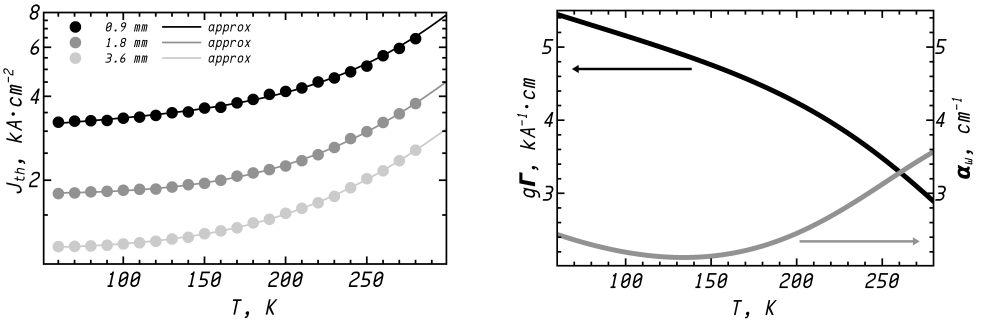

Figure 2.21: a) Measured J_{th} threshold current densities for 0.9, 1.8, and 3.6 mm length at temperature range 60-280 K.
b) Calculated temperature dependent gain coefficient and waveguide loss for QCLs devices in the temperature range 60-280 K.

For an investigation of gain and losses influences onto threshold current J_{th} the ξ function can be applied:

$$\xi(T) = \frac{d}{dT} ln(J_{th}) = \frac{1}{J_{th}(T)} \frac{dJ_{th}}{dT} \Rightarrow \tag{2.80}$$

$$= \frac{d}{dT} ln\left(J_0 \exp\left[\frac{T}{T_0}\right]\right) = \frac{d\ T/T_0}{dT} = \frac{1}{T_0}; \tag{2.81}$$

$$= \frac{d}{dT} ln\left(\frac{\alpha}{g_d^*}\right) = \frac{1}{\alpha(T)} \frac{d\alpha}{dT} - \frac{1}{g_d^*(T)} \frac{dg_d^*}{dT} = \xi_\alpha + \xi_{g_d^*}. \tag{2.82}$$

Here first part (Eq. 2.80) of equation array defines the ξ function through J_{th} variable which can be measured. Second part (Eq. 2.81) describes ξ function through characteristic temperature T_0 received from Eq. 2.75. T_0 value more often is constant for high temperatures near RT. Last part of equation array (Eq. 2.82) derived from Eq. 2.79. g_d^* variable combines $g_d\Gamma$, because experimentally Γ values is difficult to received. Moreover, optical confinement factor approximately is independent from temperature. Loss α includes waveguide α_w and mirror α_m losses. Separated ξ_α and $\xi_{g_d^*}$ part depend from losses and gain, respectively. Further, this equation allows to investigate the influence of gain and losses to temperature dependent threshold current.

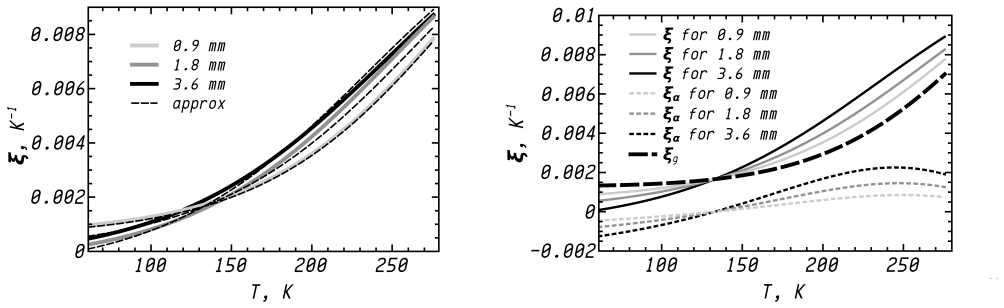

Figure 2.22: a) Calculated $\xi(T)$ parameters by $\frac{1}{J_{th}(T)} \frac{\Delta J_{th}}{\Delta T}$ (solid lines) and $\xi_\alpha + \xi_{g_d^*}$ (black dashed lines) for 0.9, 1.8, and 3.6 mm length are in light gray, gray, and black solid lines, respectively.
b) Separated $\xi_{g_d^*}$ (black dashed line) and ξ_α (short dashed lines) characteristics for 0.9, 1.8, and 3.6 mm stripe length are in light gray, gray, and black short dashed lines, respectively. Solid lines denote $\xi = \xi_{g_d^*} + \xi_\alpha$ functions for stripes equal to left figure.

$\xi(T)$ functions for 0.9, 1.8, and 3.6 mm stripe length are calculated by $\frac{1}{J_{th}(T)} \frac{\Delta J_{th}}{\Delta T}$ and are shown on Fig 2.22(a) by solid lines. From other hand $\xi(T)$ values can be received

by sum of ξ_α and $\xi_{g_d^*}$. These characteristics can be obtained from Eq. 2.82 with knowing $\alpha_w(T)$ and $g_d^*(T)$. Received values are shown by dashed lines on Fig 2.22(a). More detail representation of separated ξ_α and $\xi_{g_d^*}$ and their sum ξ are present on Fig 2.22(b). This figure shows dependence of ξ_α and $\xi_{g_d^*}$ to main characteristic ξ. ξ_α characteristic includes shift into ξ values. With increasing of cavity length L, the ξ value is increasing, which correspond to decreasing T_0 characteristic temperature. It corresponds to the result receiving in previous section and well-known experimental results. Main impact on shape of ξ is occurred from $\xi_{g_d^*}$ term at high temperatures.

According to Eq. 2.21 the gain coefficient g_d^* can be written in form:

$$\begin{gathered} g_d^* = \frac{A\Gamma C}{R_3}\frac{1}{2\gamma_{32}} \\ \text{where } A = \left(1-\frac{R_{32}}{R_2}\right),\ C = \frac{4\pi Z_{32}^2}{\lambda_0 \varepsilon_0 n_{eff} L_p},\ \text{and } R_3 = \sum R_{3i} \approx R_{32} + R_{31}. \end{gathered} \tag{2.83}$$

with scattering rate $R_i = 1/\tau_i$. In this case $\xi_{g_d^*}$ can be present in separate form for variables:

$$\begin{gathered} \xi_{g_d^*} = -\frac{d}{dT}\, ln\left(g_d^*\right) = \frac{1}{R_3(T)}\frac{dR_3}{dT} - \frac{1}{A(T)}\frac{dA}{dT} + \frac{1}{2\gamma_{32}(T)}\frac{d\,2\gamma_{32}}{dT} = \\ \xi_{R_3} + \xi_A + \xi_\gamma. \end{gathered} \tag{2.84}$$

We calculated ξ_A at range 100-280 K by temperature dependent model and received values in this range as $\sim 8 \times 10^{-5}\ K^{-1}$. The including of back filing from lowest laser level '1' by R_{12} term into rate equation increase this variable up to $\sim 8.5 \times 10^{-5}\ K^{-1}$. Fig. 2.23 shows calculated ξ_{R_3} for scatterings into lower laser levels R_{32} and R_{31} with additional scattering R_{34} into upper level '4' from upper laser level '3' (black circles). ξ_γ value was extracted from Ref. [72] and averaged as $\sim 1.4 \times 10^{-3}\ K^{-1}$.

The T_0 characteristic temperature can be evaluated from Eqs. 2.81 and 2.82 as $T_0 = (\xi_{R_3} + \xi_A + \xi_\gamma)^{-1}$. For our active region design calculated T_0 is near 143 K. Moreover, if only transition rates R_{32} and R_{31} will be taken into account for summarize R_3 the T_0 value as 357 K will be received. These results in agreement with values received by Jan

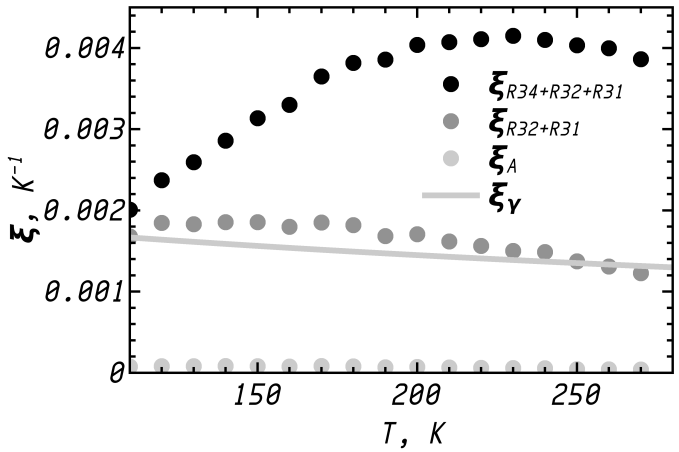

Figure 2.23: Calculated ξ_{R_3}, ξ_A, and ξ_γ (light gray line) variables for temperature range 100-280 K. Circles denote ξ characteristics calculated by temperature dependent scattering rate model.

Hellemann [73] where two very same active region designs were used with different E_{34} energy (70 meV and 150 meV). In first case the scattering R_{34} has domain impact to formation of T_0 characteristic.

3 Experimental setup and data analysis

3.1 Simulation software for scattering-rate model

For a calculation of QCL characteristics by scattering-rate models described in previous chapter the desktop and server(cluster) software are written. The GUI of desktop software is present on Fig 3.1.

Source code is written in C++ and Qt programming languages where Qt is used for generation of GUI and C++ is taken for fast calculation of mathematical problems. It allows to specify the conduction band structure by methods described in first chapter with determination of wave functions and their eigenvalues. The material for active region can be written into Table which shown on Fig 3.1. Push button ”plot design” generate conduction band profile at a given temperature and voltage. Push button ”plot WFs” generate the moduli-squared of relevant conduction band states solving Schrödinger equation by shooting method (Eq. 2.8). The gain for given energy range (Eq. 2.21) can be generated by solving rate equation (Eq. 2.15) for electron distribution calculation with previous defined transition rates by temperature dependent model introduced in previous chapter. The resulting conduction band profile with relevant moduli-squared of wave function and gain are present on Fig 3.1. Moreover, interaction information between two wave functions, such as energy difference E, dipole matrix element Z, oscillator strength f, transition time *tau*, and wavefunction overlap *Over* can be calculated and presented by GUI (Fig 3.1 [legend of bottom right window]).

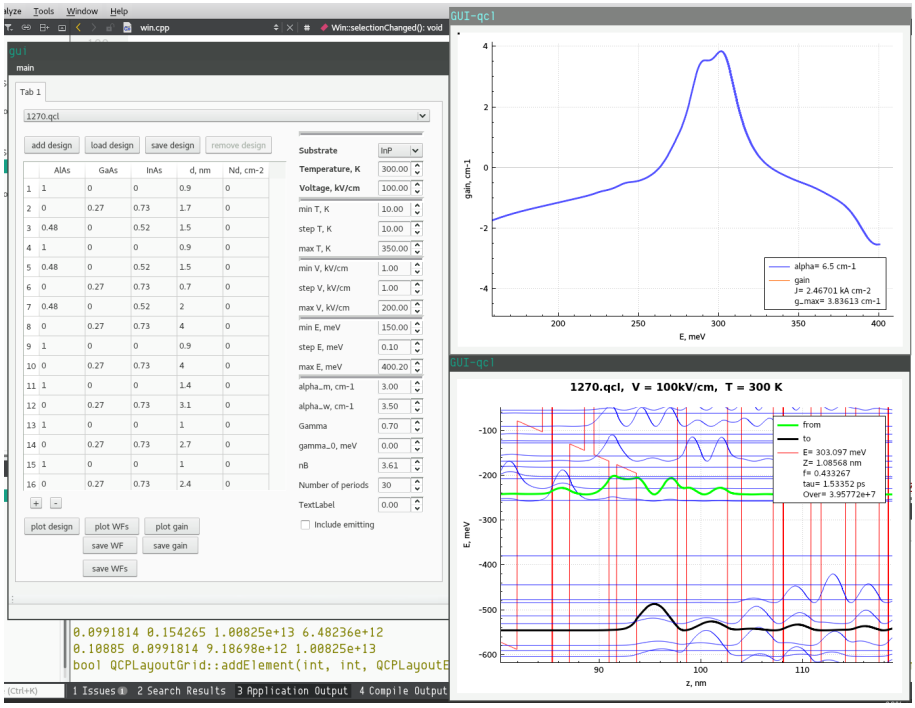

Figure 3.1: GUI of desktop software for QCL characteristics calculation. Left window is a data entry area for materials of semiconductor heterostructure of active region and for setting of temperature, voltage, and optical characteristics. Upper right window shows energy dependent gain obtained by temperature dependent scattering rate model for given temperature and voltage. Right lower window represents a portion of conduction band profile with moduli squared of the relevant wave functions. The legend shows interacting characteristics between upper and lower laser levels, which are denoted by green and black bold lines.

Further, script for calculation of temperature dependent current density-voltage-gain or current density-voltage-gain-power can be generated by desktop software by setting diapasons of temperatures and voltages and checking possibility of solutions at boundary points of ranges. This script is used by server software for calculations of temperature dependent QCL characteristics, which can be applicable for T_0 characterization, as was shown in previous chapter.

3.2 PIV measuring setup

The QCL ridge is cleaved and mounted onto a sub-mount with next attaching to copper holder with clamping contacts as shown in Fig. 3.2(a). Clamping contacts allow to control position of QCL stripe and quick mounting or removing. Fig. 3.2(b) shows mounted QCL holder onto massive copper part of cryostat, which is connect to heater/cooler RICOR K535.

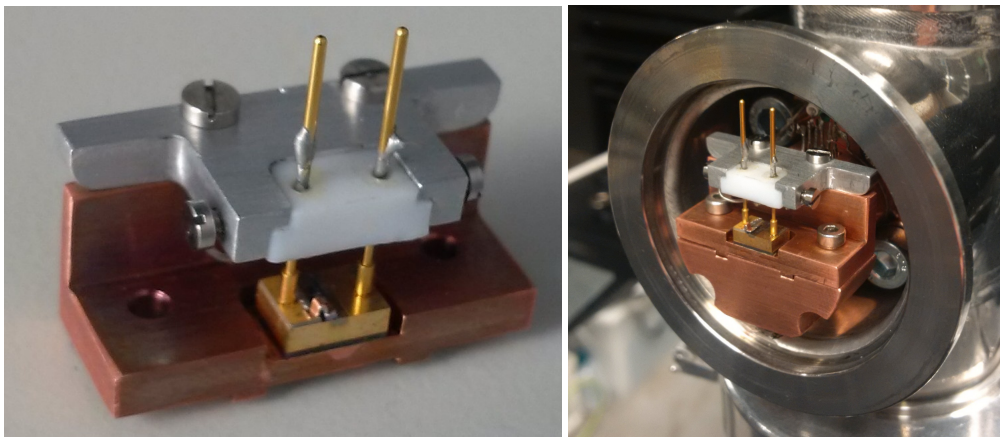

Figure 3.2: (a) Copper holder with mounted QCL sample and clamping contacts.
(b) Mounted copper QCL holder to massive copper cryostat part with temperature control.

The schematic power-current-voltage measuring setup is present in Fig. 3.3 for temperature dependent characterization. The Avtech AV-107C-B is used as current source. Current pulses of 150 ns width and low duty cycles (1.5%) which used in order to avoid laser heating.

The current and the voltage signals are monitored using digital oscilloscope Picoscope 4425 with 4 fully differential high-impedance inputs. The average output power is measured using a thermopile detector placed in front of the laser facet separated by sapphire windows. The chopper synchronizes the current source and power detector with 30 Hz frequency. Moreover, the optical power is monitored by oscilloscope too. Average over 1 second values of current, voltage, power, and temperature are sent to a laptop for collection and data processing.

Measurement setup works in temperature diapason from 40 K to 300 K. The control

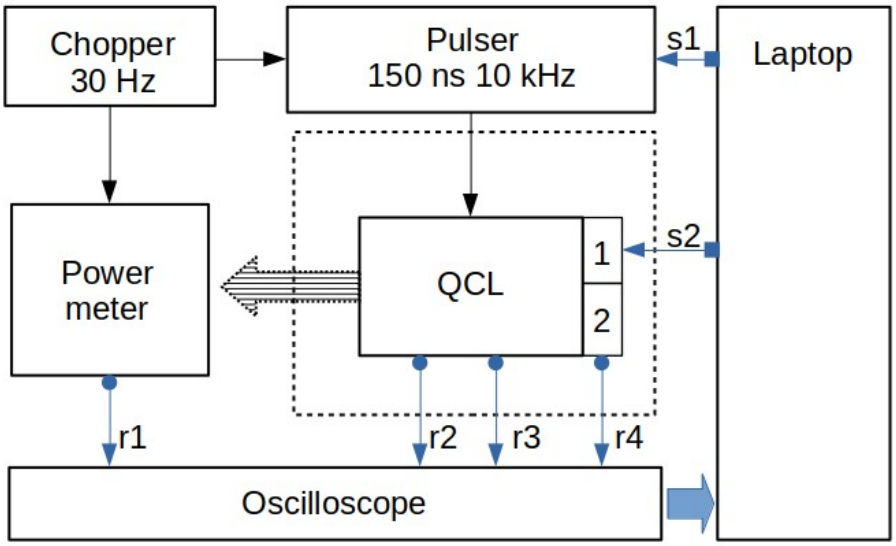

Figure 3.3: Standard schematic setup for power-current-voltage measurements in pulse operation between 40 and 300 K. The sample ("QCL" box) is mounted in a cryostat (dashed box) with vacuum about 10^{-5}-10^{-6} mbar. Current pulser and power meter are synchronized by chopper with frequency 30 Hz (dashed arrows). Oscilloscope collect power ($r1$), current ($r2$), voltage ($r3$), and temperature ($r4$) data followed by laptop. The laptop controls current ($s1$) and temperature ($s2$). Boxes 1 and 2 denote temperature control part of RICOR K535 and temperature resistant, respectively.

of accuracy for measuring temperature is improved to ± 0.5 K (factory value is ± 2 K) and is implemented from laptop through RS-232 hardware interface. Moreover, the recommended step for measurements is 10 K. The current range for Avtech current source is from 0 to 10 A with 0.01 A step with laptop controlling COM-port. Based on this opportunity, software is written for power-current-voltage measurements for different temperatures. The GUI is present in Fig. 3.4.

The option "maximum power" (max_P) is useful for T_0-measurements when dynamical range of current is applicable. At the end of a measurement the data can be saved to files in specified directory for further treatment. Next code-scripts allow extract $J_{th}(T)$, T_0, and T_1 characteristics which are not observed in this section.

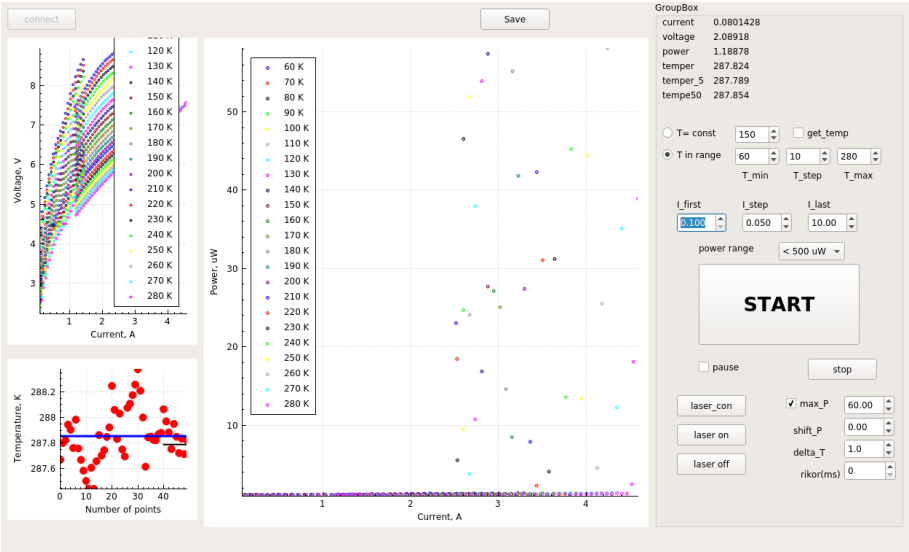

Figure 3.4: GUI for carrying out PIV measurements in pulse operation between 40 and 300 K.

3.3 Experimental current-voltage characteristics of QCLs

Often measured data consist non clean information. For example, measured optical power has losses on optical windows in cryostat and scatterings on different surfaces, absorption in air (MIR- spectrum), *etc*. For electrical measurements the external resistivity in metal wires or electrical contact and *etc.* are always present. In contrast with measurements, simulation processes are considered as ideal. The quality of comparison measured data and simulation directly depend from extraction of unnecessary additional values in data.

3.3.1 Experimental IV characteristics for different size of laser ridge

So experimental setup can't be ideal as simulations. Noises with additional resistances always present in results.

With this information and knowing that voltage from QCL devices is received with additional values, the experimental data always needs to correct.

IV characteristics of QCL devices with 2, 4 and 8 mm long were measured by setup

described in previous section. The devices were mounted in a liquid nitrogen cryostat for measurements and driven by 150 ns pulses with low duty-cycle (1.5 %). Received IV characteristics are presented in Fig. 3.5(a).

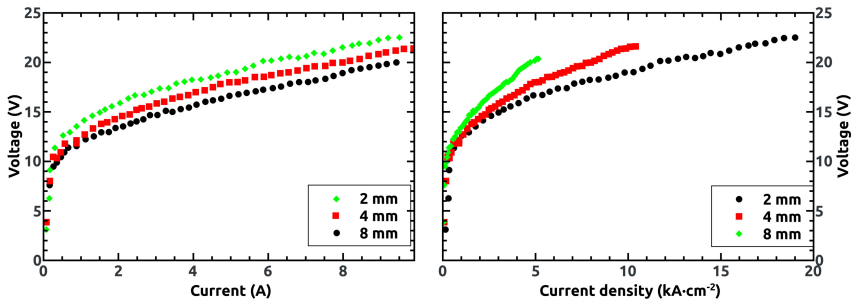

Figure 3.5: Experimental current-voltage (a) and current density - voltage (b) characteristics at 80 K for 2, 4 and 8 mm long devices using the active region same to QCL design presented in Fig. 2.6.

IV characteristics for these samples have similar values, but after calculation to the current density - voltage the dependencies are not consistent with the idea that J-V characteristic of QCL active region is independent from geometric of laser stripe.

The external voltage U_{external} and resistance R_{external} can be find for series of QCL ridges with different length:

$$\begin{aligned} U_{\text{exp}}(I) &= U_{\text{QCL}}(I) + U_{\text{external}}(I) = U_{\text{QCL}}(I) + R_{\text{external}} \cdot I, \\ U_{\text{exp}}(J) &= U_{\text{QCL}}(J) + R_{\text{external}} W_{\text{QCL}} J \cdot L_{\text{QCL}}, \end{aligned} \tag{3.1}$$

where U_{exp}, I, J are measured voltage, current, and current density, respectively. U_{QCL} demotes voltage created on QCL active region with W_{QCL} width and L_{QCL} stripe length.

In our case, for three devices with different length (2, 4, 8 mm) Eq. 3.1 can be rewritten as system of equations:

$$\begin{aligned} U_2(J) &= U_{\text{QCL}}(J) + 0.2 \cdot R_{\text{external}} J W_{\text{QCL}}, \\ U_4(J) &= U_{\text{QCL}}(J) + 0.4 \cdot R_{\text{external}} J W_{\text{QCL}}, \\ U_8(J) &= U_{\text{QCL}}(J) + 0.8 \cdot R_{\text{external}} J W_{\text{QCL}}, \end{aligned} \tag{3.2}$$

where $U_{\text{QCL}}(J)$ and R_{noise} are two unknown quantities. External resistivity R_{external} will

be fitted from this system of equations. Current density – voltage $U_{\mathrm{QCL}}(J)$ characteristic is our goal which can be found from any model which can calculate this characteristic or can be found from this system equation.

Cleared measured $U_i(J)$ and calculated $U_{\mathrm{QCL}}(J)$ voltage-current density characteristic by phenomenological scattering rate model are present in Fig. 3.6.

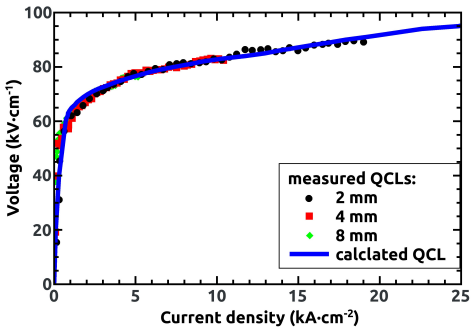

Figure 3.6: Fitted U_{QCL} for 2, 4, and 8 long devices are by black, red, and green dots, respectively. Blue line denote calculated J-V characteristic.

The value of R_{external} ≈0.53 Ω was fitted from system of equations. With this information results, from measured data have good agreement with simulation. Founded U_{QCL} for 8, 4, and 2 long devices are shown in Fig. 3.6 (b) with comparison calculated values which denoted by green asterisks.

3.3.2 Thermal experimental IV characteristics

Previously the external resistent is received only at 80 K. Temperature dependent characteristic $R_{external}(T)$ is more suitable for analysis of experimental IV data. Moreover, the form of temperature dependence could explain type of external resistance. Fig. 3.7 shows experimental IV characteristics for QCL devices. The threshold voltage drop between 80 K and 300 K is about 6 V with expected less than 2 V. Also voltages near "max power" current should be same values.

Taking it into account, the Eq. 3.1 may be written for temperature range as:

$$U_{\mathrm{exp}}(J,T) = U_{\mathrm{QCL}}(J,T) + R_{\mathrm{external}}(T)\cdot J \tag{3.3}$$

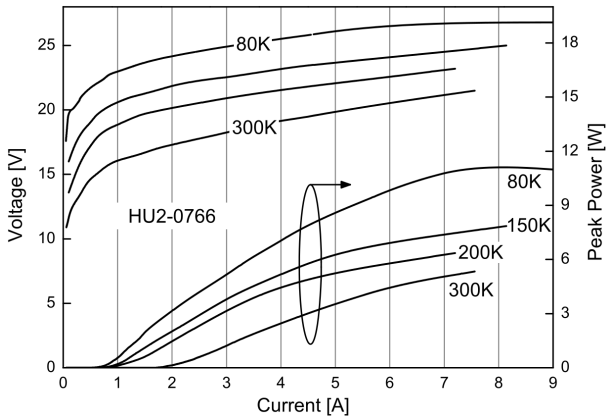

Figure 3.7: Voltage-current and light-output characteristics for a 25 μm $\times$ 3.0 mm QCL sample of structure observed in Ref. [36]. The device was driven with 300 ns $\times$ 10 kHz current pulses at different heat sink temperatures.

We investigated the IV characteristics of 0.9. 1.8, and 3.6 mm length devices with the active region observed in previous section, see Fig. 2.19. The equation system (Eq. 3.3) was solved at different temperatures. The dependence of fitted external resistance at 60-260 K range is present in Fig. 3.8.

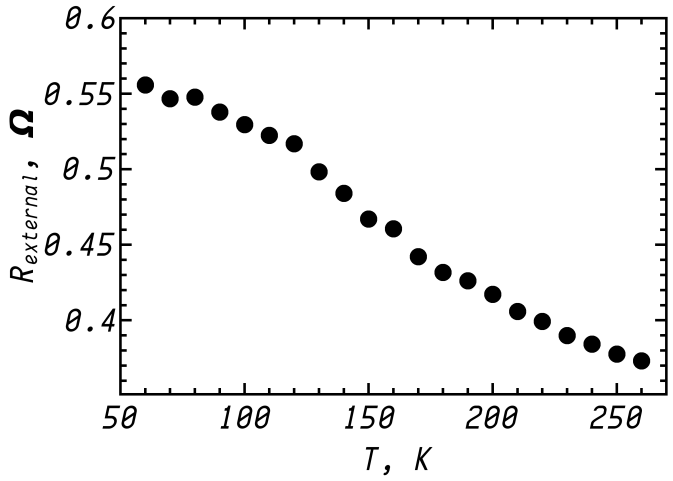

Figure 3.8: Fitted external resistance at different temperatures extracted from measured IV characteristics for 0.9, 1.8, and 3.6 mm devices with active region presented in Fig. 2.19.

The values for this and previous experiments at 80 K were received after reassembly of equipment with replacement of metal wires. Moreover the recession of external resistance shows non-metal temperature dependence. Main place for this resistance can be in

metal-semiconductor or semiconductor-semiconductor contacts.

---

4 Conclusions and perspectives

This thesis investigates electron scattering processes in quantum cascade lasers and their influence on devices characteristics. At the beginning we introduced compact phenomenological scattering-rate model for vertical electron transport in QCL active region at low temperatures. This model present transition rate as a product of energy dependent factor and overlap integral for the squared moduli of the envelope functions. Due to to good agreement with experimental results and comparison with other model, this compact model can be used in design and optimization of QCL structures at low temperatures.

Afterwords we considered temperature effects on main types of scattering processes in QCLs. The temperature dependent transition rate for phonons and interface roughness were derived from the corresponding Hamiltonian and presented in product form of energy dependent factor and overlap integral. Moreover, the overlap integral for IFR corresponds to sum of the squared moduli of the envelope functions on interfaces. According to assumption that overlap of wave functions does not change much with temperature, the energy dependent factor is investigated for different temperatures.

As the main goal of any model is describing or prediction of an experiment, we applied the temperature dependent model to the characterization of T_0 characterization temperature of QCLs. The gain-current density characteristics for broad temperature range were calculated for specific QCL active region. Calculated T_0 characteristic was obtained as a function of an electron sheet density per period and losses in gain medium. Moreover, the influence of optical confinement factor to T_0 is investigated. Finally, the electron sheet density per period was fitted for experimental loss values. The obtained vale agrees well

with doping calibration.

At the end of this research, we investigated the influence of gain and losses on T_0 separately and defined the main influence of gain on this characteristic.

In this research, the scattering into continuum wasn't considered, which takes place at high temperatures. Unfortunately, it is one of the main leakage for THz QCLs which still don't work at RT. And as of next step, this type of scattering should be included into the developed model. Also T_1 characteristic for describing of laser power efficiency dependence is not investigated in this research but in the process.

Bibliography

[1] J. Faist, F. Capasso, D. L. Sivco, C. Sirtori, A. L. Hutchinson, and A. Y. Cho, Science **264**, 553 (1994).

[2] Y. Yao, A. J. Hoffman, and C. F. Gmachl, Nat. Photon. **6**, 432 (2012).

[3] S. Slivken, A. Evans, W. Zhang, and M. Razeghi, Appl. Phys. Lett. **90**, 151115 (2007).

[4] M. Razeghi, S. Slivken, Y. Bai, B. Gokden and S. R. Darvish, New J. Phys. **11**, 125017 (2009).

[5] J. D. Kirch, C.-C. Chang, C. Boyle, L. J. Mawst, D. Lindberg III, T. Earles, and D. Botez, Appl. Phys. Lett. **106**, 151106 (2015).

[6] D. Botez, C.-C. Chang, L. J. Mawst, J. Phys. D: Appl. Phys. **49** (4), 043001 (2016).

[7] J. Faist, C. Gmachl, F. Capasso, C. Sirtori, D. L. Sivco, J. N. Baillargeon, and A. Y. Cho, Appl. Phys. Lett. **70**, 2670 (1997).

[8] N. Yu, R. Blanchard, J. Fan, F. Capasso, T. Edamura, M. Yamanishi, and H. Kan, Appl. Phys. Lett. **93**, 181101 (2008).

[9] J. Faist, F. Capasso, D. L. Sivco, A. L. Hutchinson, C. Sirtori, and A. Y. Cho, Infrared Phys. Technol. **36**, 99 (1995).

[10] C. Gmachl, F. Capasso, D. L. Sivco, and A. Y. Cho, Rep. Prog. Phys. **64**, 1533 (2001).

[11] K. Namjou, S. Cai, E. A. Whittaker, J. Faist, C. Gmachl, F. Capasso, D. L. Sivco, and A. Y. Cho, Optics Letters. **23**, 219, 3 (1998).

[12] A. Wacker, Phys. Rev. B **66**, 085326 (2002).

[13] S.-C. Lee and A. Wacker, Phys. Rev. B **66**, 245314 (2002).

[14] R. C. Iotti and F. Rossi, Phys. Rev. Lett. **87**, 146603 (2001).

[15] T. Kubis, C. Yeh, P. Vogl, A. Benz, G. Fasching, and C. Deutsch, Phys. Rev. B **79**, 195323 (2009).

[16] A. Wacker, M. Lindskog, and D. O. Winge, IEEE J. Sel. Top. Quantum Electron. **19**, 1 (2013).

[17] P. Y. Yu, M. Cardona, *Fundamentals of Semiconductors* (4rd Edition, Springer, Berlin, Heidelberg 2010).

[18] I. Vurgaftman, J. R. Meyer, and L. R. Ram-Mohan, J. Appl. Phys., **89**, 11, 5815 (2001).

[19] Yu. A. Goldberg and N. M. Schmidt, Handbook Series on Semiconductor Parameters, **vol.2**, M. Levinshtein, S. Rumyantsev and M. Shur, ed., World Scientific, London, **1999**, pp. 62-88.

[20] C. G. Van de Walle and R. M. Martin, Phys. Rev. B **34**, 5621 (1986).

[21] C. G. Van de Walle and R. M. Martin, Phys. Rev. B **35**, 8154 (1987).

[22] M. L. Cohen, J. Chelikowsky, *Electronic Structure and Optical Properties of Semiconductors*, Solid-State Sci., Vol.**75** (2nd Edition, Springer, Berlin, Heidelberg 1989)

[23] N. Trouillier, J. L. Martins, Phys. Rev. B **43**, 1993 (1991)

[24] D. J. Chadi, M. L. Cohen, Phys. Stat. Solidi B **68**, 405 (1975)

[25] E. O. Kane, J. Phys. Chem. Solids **1**, 249–261 (1957).

[26] Y. P. Varshni, Physica (Amsterdam) **34**, 149 (1967).

[27] C. G. Van de Walle, Phys. Rev. B, **39**(3) (1989).

[28] J. H. Davies, *The Physics of Low-Dimensional Semiconductors*, (Cambridge University Press, Cambridge, 1997).

[29] W. A. Harrison, Phys. Rev. **104**, 1281 (1956).

[30] C. Y. Chang and F. Kai, *GaAs High-Speed Devices* (John Wiley and Sons, New York, 1994).

[31] J. H. Smet, C. G. Fonstad, and Q. Hu. J. Appl. Phys., **79**, 12, 9305 (1996).

[32] K. Donovan, P. Harrison, and R. W. Kelsall, J. Appl. Phys. **89**, 3084 (2001).

[33] P. Harrison, *Quantum Wells, Wires and Dots* (3rd Edition, Wiley, Chichester, 2009).

[34] C. Jirauschek and T. Kubis, Appl. Phys. Rev. **1**, 011307 (2014).

[35] R. Nelander and A. Wacker, J. Appl. Phys. 106, 063115 (2009).

[36] Y. V. Flores, S. S. Kurlov, M. Elagin, M. P. Semtsiv, and W. T. Masselink, Appl. Phys. Lett. **103**, 161102 (2013)

[37] Y. T. Chiu, Y. Dikmelik, P. Q. Liu, N. L. Aung, J. B. Khurgin, and C. F. Gmachl, Appl. Phys. Lett. **101**, 171117 (2012)

[38] J. B. Khurgin, Y. Dikmelik, P. Q. Liu, A. J. Hoffman, M. D. Escarra, K. J. Franz, and C. F. Gmachl, Appl. Phys. Lett. **94**, 091101 (2009)

[39] M. P. Semtsiv, Y. Flores, M. Chashnikova, G. Monastyrskyi, and W. T. Masselink, Appl. Phys. Lett. **100**, 163502 (2012)

[40] T. Unuma, T. Takahashi, T. Noda, M. Yoshita, H. Sakaki, M. Baba, and H. Akiyama, Appl. Phys. Lett. **78**, 3448 (2001).

[41] J. B. Khurgin, Appl. Phys. Lett. 93, 091104 (2008).

[42] R. F. Kazarinov and R. A. Suris, Sov. Phys. Semicond. **5**, 207 (1971).

[43] D. Indjin, P. Harrison, R. W. Kelsall, and Z. Ikonic, J. Appl. Phys. **91**, 9019 (2002).

[44] L. Schrottke, M. Giehler, M. Wienold, R. Hey, and H. T. Grahn, Semicond. Sci. Technol. **25**, 045025 (2010).

[45] C. Peng, G. Chen, T. Yang, S.-W. Park, and R. Martini, Semicond. Sci. Technol. **28**, 105008 (2013).

[46] K. Choi, B. Levine, R. Malik, J. Walker, and C. Bethea, Phys. Rev. B. **35**, 4172 (1987).

[47] J. Faist, *Quantum Cascade Lasers* (Oxford University Press, Oxford, 2013).

[48] J. Faist, D. Hofstetter, M. Beck, T. Aellen, M. Rochat, and S. Blaser, IEEE J. Quantum Electron. **38**, 533 (2002).

[49] J. Faist, F. Capasso, C. Sirtori, D. L. Sivco, J. N. Baillargeon, A. L. Hutchinson, S.-N. G. Chu, and A. Y. Cho, Appl. Phys. Lett. **68**, 3680 (1996).

[50] C. Sirtori, P. Kruck, S. Barbieri, P. Collot, J. Nagle, M. Beck, J. Faist, and U. Oesterle, Appl. Phys. Lett. **73**, 3486 (1998).

[51] D. Hofstetter, M. Beck, T. Aellen, and J. Faist, Appl. Phys. Lett. **78**, 396 (2001).

[52] J. Faist, M. Beck, T. Aellen, and E. Gini, Appl. Phys. Lett. **78**, 147 (2001).

[53] G. Scamarcio, F. Capasso, C. Sirtori, J. Faist, A. L. Hutchinson, D. L. Sivco, and A. Y. Cho, Science **276**, 773 (1997).

[54] G. Scamarcio, F. Capasso, J. Faist, C. Sirtori, D. L. Sivco, A. L. Hutchinson, and A. Y. Cho, Phys. Lett. **70**, 1796 (1997).

[55] A. Tredicucci, F. Capasso, C. Gmachl, D. Sivco, A. Hutchinson, and A. Cho, IEEE Photon. Technol. Lett. **12**, 260 (2000)

[56] L. Schrottke, M. Wienold, M. Giehler, R. Hey, and H. T. Grahn, J. Appl. Phys. **108**, 103108 (2010).

[57] D. Botez, S. Kumar, J. C. Shin, L. J. Mawst, I. Vurgaftman, and J. R. Meyer, Appl. Phys. Lett. **97**, 071101 (2010).

[58] A. Vasanelli, A. Leuliet, C. Sirtori, A. Wade, G. Fedorov, D. Smirnov, G. Bastard, B. Vinter, M. Giovannini, and J. Faist, Appl. Phys. Lett. **89**, 172120 (2006).

[59] R. Nelander and A. Wacker, Appl. Phys. Lett. **92**, 081102 (2008).

[60] A. Y. Song, R. Bhat, P. Bouzi, C.-E. Zah, and C. F. Gmachl, e-print arXiv:1507.06016.

[61] C. Sirtori, J. Faist, F. Capasso, D. L. Sivco, A. L. Hutchinson, S. N. G. Chu, and A. Y. Cho, Appl. Phys. Lett. **68**, 1745 (1996).

[62] C. Sirtori, J. Faist, F. Capasso, D. L. Sivco, A. L. Hutchinson, and A. Y. Cho, Appl. Phys. Lett. **69**, 2810 (1996).

[63] M. Fischer, G. Scalari, K. Celebi, M. Amanti, Ch. Walther, M. Beck, and J. Faist, Appl. Phys. Lett. **97**, 221114 (2010).

[64] C. Sirtori, J. Faist, F. Capasso, D. L. Sivco, A. L. Hutchinson, and A. Y. Cho, Appl. Phys. Lett. **66**, 3242 (1995).

[65] C. Gmachl, F. Capasso, J. Faist, A. L. Hutchinson, A. Tredicucci, D. L. Sivco, J. N. Baillargeon, S. N. G. Chu, and A. Y. Cho, Appl. Phys. Lett. **72**, 1430 (1998).

[66] C. Gmachl, A. Tredicucci, F. Capasso, A. L. Hutchinson, D. L. Sivco, J. N. Baillargeon, and A. Y. Cho, Appl. Phys. Lett. **72**, 3130 (1998).

[67] C. Gmachl, F. Capasso, A. Tredicucci, D. L. Sivco, A. L. Hutchinson, S. N. G. Chu, and A. Y. Cho, Appl. Phys. Lett. **73**, 3830 (1998).

[68] A. Wittmann, Y. Bonetti, J. Faist, E. Gini, and M. Giovannini, Appl. Phys. Lett. **93**, 141103 (2008).

[69] Y. V. Flores, *"Mid-Infrared Quantum Cascade Lasers: Theoretical and Experimental Studies on Temperature-Driven Scattering"*. Ph. D. thesis, Humboldt-Universität zu Berlin (2014).

[70] M. P. Semtsiv, W. T. Masselink, Appl. Phys. Lett. **109**, 203502 (2016).

[71] Y. Flores, M. P. Semtsiv, M. Elagin, G. Monastyrskyi, S. Kurlov, A. Aleksandrova, J. Kischkat, and W. T. Masselink, J. Appl. Phys. **113**, 134506 (2013).

[72] Z. Liu, C. F. Gmachl, L. Cheng, F.-S. Choa, F. J. Towner, X. Wang, and J. Fan, J. Quantum Electron. **44**, 5 (2008).

[73] J. Hellemann, *"Thermal Characterization and Processing of Mid Infrared Quantum Cascade Lasers"*. M. Sc. thesis, Humboldt-Universität zu Berlin (2017).